

35 **Abstract**

36 Radial spokes (RS) are T-shaped multiprotein complexes on the axonemal microtubules.
37 Repeated RS1, RS2, and RS3 couple the central pair to modulate ciliary and flagellar motility.
38 Despite the cell type specificity of RS3 substructures, their molecular components remain largely
39 unknown. Here, we report that a leucine-rich repeat-containing protein, LRRC23, is an RS3 head
40 component essential for its head assembly and flagellar motility in mammalian spermatozoa.
41 From infertile male patients with defective sperm motility, we identified a splice site variant of
42 *LRRC23*. A mutant mouse model mimicking this variant produces a truncated LRRC23 at the C-
43 terminus that fails to localize to the sperm tail, causing male infertility due to defective sperm
44 motility. LRRC23 was previously proposed to be an ortholog of the RS stalk protein RSP15.
45 However, we found that purified recombinant LRRC23 interacts with an RS head protein RSPH9,
46 which is abolished by the C-terminal truncation. Evolutionary and structural comparison also
47 shows that LRRC34, not LRRC23, is the RSP15 ortholog. Cryo-electron tomography clearly
48 revealed that the absence of the RS3 head and the sperm-specific RS2-RS3 bridge structure in
49 LRRC23 mutant spermatozoa. Our study provides new insights into the structure and function of
50 RS3 in mammalian spermatozoa and the molecular pathogenicity of LRRC23 underlying reduced
51 sperm motility in infertile human males.
52

53 Introduction

54

55 Motile cilia and flagella are evolutionarily conserved organelles essential for cellular motility
56 (Inaba, 2011; Ishikawa, 2017). The core of motile cilia and flagella is the '9+2' axoneme,
57 characterized by a scaffold structure composed of nine peripheral microtubule doublets (MTDs)
58 and a central pair of singlet microtubules (CP). Each MTD binds two rows of dyneins, the outer-
59 arm dyneins (OAD) and inner-arm dyneins (IAD), which generate mechanical force required for
60 the ciliary beating via ATP hydrolysis (Kubo *et al.*, 2021; Rao *et al.*, 2021). Radial spoke (RS)
61 controls the amplitude of the ciliary and flagellar beat by transmitting mechanochemical signals
62 from the CP to the axonemal dyneins (Smith & Yang, 2004; Viswanadha *et al.*, 2017). In
63 *Chlamydomonas reinhardtii*, RS mutations paralyze the flagellar movement (Witman *et al.*, 1978)
64 and the axoneme lacking RS system shows reduced velocity of microtubule sliding by dyneins
65 (Smith & Sale, 1992). In human and mouse, mutations in RS components or their absence cause
66 primary ciliary dyskinesia (PCD) and/or male infertility due to the defective ciliary and flagellar
67 beating (Abbasi *et al.*, 2018; Liu *et al.*, 2021; Sironen *et al.*, 2020). These studies highlight the
68 physiological importance of RS in regulating ciliary and flagellar movement.

69

70 A triplet of three RSs (RS1, RS2, and RS3) repeats every 96-nm along the peripheral MTDs and
71 this 96-nm periodicity of RS is well-conserved in cilia and flagella across diverse organisms
72 (Viswanadha *et al.*, 2017; Zhu *et al.*, 2017). RS is a multiprotein complex; at least 23 RS
73 components were identified in *C. reinhardtii* (Gui *et al.*, 2021; Viswanadha *et al.*, 2017; Yang *et al.*,
74 2006). These RS components are also crucial for RS organization and function in other ciliated
75 and flagellated organisms (Bazan *et al.*, 2021; Ralston *et al.*, 2006; Sironen *et al.*, 2020; Urbanska
76 *et al.*, 2015), indicating evolutionarily conserved molecular composition of the RS. However, cryo-
77 electron microscopy (cryo-EM) studies have revealed species- and tissue-specific structural
78 variabilities in RS3. For example, RS3 in most species is a T-shaped axonemal structure that
79 consists of a head and a stalk like those of RS1 and RS2 (Imhof *et al.*, 2019; Leung *et al.*, 2021;
80 Lin *et al.*, 2014; Pigino *et al.*, 2011) but RS3 in *C. reinhardtii* is a headless and stump-like structure
81 (Pigino *et al.*, 2011). In addition, mammalian sperm flagellar axoneme carries a unique bridge
82 structure between RS2 and RS3 (Leung *et al.*, 2021), which is not observed from tracheal cilia as
83 well as other flagellated organisms (Imhof *et al.*, 2019; Lin *et al.*, 2014). This variability suggests
84 that RS3 is an evolutionarily more divergent structure and conveys species- and/or tissue-specific
85 ciliary and flagellar function. Yet, the overall molecular composition of RS3 and the extent to
86 which RS3 components are species- and/or tissue specific remains largely unknown.

87

88 Asthenozoospermia (ASZ) is the male infertility classified by reduced sperm motility (World
89 Health Organization, 2010). ~80% of male infertile patients manifest sperm motility defects (Curi
90 *et al.*, 2003) as infertile male with abnormal sperm morphology and/or reduced sperm count often
91 accompany low motility (Cavarocchi *et al.*, 2022; Toure *et al.*, 2021). Recent whole exome
92 sequencing studies identified genetic defects in RS components from idiopathic ASZ patients (Liu
93 *et al.*, 2021; Martinez *et al.*, 2020; Shen *et al.*, 2021). Mutant analyses using model organisms
94 further elucidated the function of RS components in the flagellar movement and the pathogenic
95 mechanisms (Liu *et al.*, 2021; Martinez *et al.*, 2020). Thus, WES combined with functional and
96 structural analyses of mutants, especially in a mouse model, would be a powerful and direct
97 approach to understand mammalian specific RS3 roles including sperm motility regulation and
98 genetic etiologies causing male infertility.

99

100 Here, we report a bi-allelic loss-of-function splicing variant in *LRRC23* from ASZ patients in a
101 Pakistani consanguineous family. We generated a mouse model that mimics the human mutation
102 and found that the mutation leads to C-terminal truncated *LRRC23* and that the mutant mice

103 phenocopy the impaired sperm motility and male infertility. Using biochemical analyses and
104 structural prediction, we showed that, different from previously known, LRRC23 is not the
105 ortholog of a RS2 stalk protein RSP15 but interacts with a known RS head protein. Finally, we
106 visualized the in-cell structures of RS triplets in intact WT and mutant sperm using cryo-electron
107 tomography (cryo-ET). We observed missing RS3 head and aberrant junction between RS2 and
108 RS3 in the mutant flagellar axoneme, unarguably demonstrating that LRRC23 is a head
109 component of RS3. This study provides molecular pathogenicity of *LRRC23* in RS-associated
110 ASZ and reveals unprecedented structural insights into the RS3 and its implication in normal
111 sperm motility and male fertility in mammals.
112
113

114 Results

115

116 A Loss of Function Splice Site Variant Truncating LRRC23 is Identified from a 117 Consanguineous Family with Asthenozoospermia

118 A consanguineous Pakistani family with infertile males was recruited (Fig 1 A). Both infertile
119 males (IV-1 and IV-2) have failed to have child over 3 years of unprotected sex after marriage
120 (Table EV1). The male infertile patients do not show PCD-related symptoms, abnormal heights,
121 weights, secondary characteristics, nor anatomical defects. They also have normal karyotypes
122 without Y chromosome microdeletion. Overall, the Papanicolaou (PAP) stained spermatozoa from
123 the infertile patients showed an overall normal morphology (Figs 1B and EV1A), which was
124 further supported by normal ranges of abnormal sperm morphology assessed by clinical semen
125 analysis (Table EV1). However, their progressive motility was lower than the World Health
126 Organization (WHO) standard (World Health Organization, 2010) and the patients were clinically
127 diagnosed as ASZ (Table EV1). To understand the genetic etiology underlying the defective
128 sperm motility, we performed whole exome sequencing (WES) on the proband, IV-1. WES
129 estimated 5.02% inbreeding co-efficiency and the longest homozygous-by-descent segment as
130 37.5 cM, verifying the consanguineous nature of the recruited family. Among the four identified
131 rare variants (Table EV2), only one homozygous splicing donor site variant (c.621+1G>A) in
132 *LRRC23* (leucin-rich repeat containing protein 23) is co-segregated with the male infertility
133 phenotype (Fig 1A, C, and D). Of note, a female sibling (IV-4) who also has the homozygous
134 *LRRC23* variant (IV-4) is infertile because her partner was able to have children from his second
135 marriage (Fig 1A). However, the infertility of IV-4 is not likely be due to the variant because the
136 mother (III-1) also carries the homozygous allele but was fertile (Fig 1A). The variant at the
137 splicing donor site of *LRRC23* intron 5 is predicted to prevent splicing out of the intron, which can
138 lead to early termination of protein translation with loss of 136 amino acids at the C-terminus (Fig
139 EV1B and C). To verify the splicing defects and generation of mutant protein by the variant, we
140 constructed minigenes to express *LRRC23* ORF spanning partial intron 5 with the normal or
141 variant sequence at the splicing site in 293T cells (Fig 1E). 293T cells transfected with the
142 construct carrying the variant failed to splice out the intronic region (Fig 1F) and generated only
143 truncated LRRC23 (Fig EV1D). These results suggest the variant is pathogenic and explains the
144 male infertility with defective sperm motility in this family.

145

146 C-terminally Truncated LRRC23 Fails to Localize in the Flagella and Causes Defective 147 Sperm Motility

148 *LRRC23* is a radial spoke (RS) component (Padma *et al*, 2003). Consistent with the ASZ
149 phenotype in our infertile patients with a new splice mutation in *LRRC23*, genetic ablation of
150 *Lrrc23* in mice causes severe sperm motility defects and male infertility (Zhang *et al*, 2021).
151 However, how the C-terminus truncation of *LRRC23* affects the RS structure and function
152 remains unresolved. To better understand detailed function of *LRRC23* and the molecular
153 pathogenicity of the identified variant, we generated *Lrrc23* mutant mice by CRISPR/Cas9
154 genome editing to mimic the predicted outcome in human patients (Figs EV1 and EV2A). We
155 targeted two regions, one in intron 5 and the other in intron 7 (Fig EV2B) to delete exon 6 and 7
156 together and express truncated *LRRC23* at C-terminus. We established two mouse lines with
157 4,126 or 4,135 bp deletion (*Lrrc23-4126del* and *Lrrc23-4135del*, respectively) (Fig EV2C). Both
158 homozygous *Lrrc23-4126del* and *4135del* mice displayed the identical male infertility and
159 defective sperm motility phenotypes in our initial characterization. In this study, we used *Lrrc23-4126del*
160 line as *Lrrc23-mutant* line unless indicated. We observed that truncated *Lrrc23* mRNA is
161 expressed from the mutant *Lrrc23* allele but the total mRNA level of *Lrrc23* in testis is not different
162 from wildtype (WT) to that in *Lrrc23*^{ΔΔ} males (Fig EV2D-F). Sequencing the truncated *Lrrc23*
163 mRNA revealed that the transcript would produce mutant LRRC23 containing 27 non-native

164 amino acids translated from 3' UTR instead of 136 amino acids at the C-terminus (Fig EV2G).
165 Despite the comparable *Lrrc23* mRNA levels in WT and *Lrrc23*^{ΔΔ} testis, the truncated LRRC23 is
166 detected only marginally in the microsome fraction of *Lrrc23*^{ΔΔ} testis, different from full-length
167 LRRC23 enriched in the cytosolic fraction of WT testis (Figs 2A and EV3A and B). In addition, the
168 mutant LRRC23 is not present in epididymal sperm (Figs 2B and C, and EV3C-E), indicating that
169 the C-terminal region is essential for proper LRRC23 transportation to the sperm flagella.

170
171 Sperm from *Lrrc23*^{ΔΔ} and *Lrrc23-4135del*^{ΔΔ} males are morphologically normal (Figs 2C and
172 EV3E and F) and the epididymal sperm counts of *Lrrc23*^{+/Δ} and *Lrrc23*^{ΔΔ} males are not
173 significantly different (Fig 2D). Despite the normal morphology and sperm counts, *Lrrc23*^{ΔΔ} males
174 are 100% infertile (Fig 2E and F). By contrast, *Lrrc23*^{ΔΔ} females are fertile, which supports the IV-
175 4's infertility is not likely due to the identified variant (Fig 1A). To further understand how the
176 homozygous *Lrrc23* mutation causes male infertility, we performed Computer Assisted Semen
177 Analysis (CASA). *Lrrc23*^{ΔΔ} sperm motility parameters are significantly altered compared to
178 *Lrrc23*^{+/Δ} sperm (Fig EV3G). *Lrrc23*^{ΔΔ} sperm cannot swim efficiently under viscous conditions that
179 mimic the environment in female reproductive tract (Fig 2G; Movie EV1), and their flagella just
180 vibrate but do not beat normally (Figs 2H and EV3H; Movie EV2). In addition, inducing
181 capacitation did not rescue any observed motility defect of *Lrrc23*^{ΔΔ} sperm as demonstrated by
182 flagellar waveform analysis, and CASA measurement of curvilinear velocity (VCL), straight line
183 velocity (VSL), and amplitude of lateral head (ALH). These results suggest the C-terminal
184 truncation dysregulates the flagellar localization of the mutant LRRC23, leading to sperm motility
185 defects and male infertility.

186
187 **C-terminal Truncation of LRRC23 Abolishes its Interaction with Radial Spoke Head**
188 Recent cryo-ET studies revealed that T-shaped RS structures (i.e., head and stalk) are conserved
189 across the species (Leung *et al.*, 2021; Lin *et al.*, 2014) (Fig. 3 A). Three RSs (RS1, RS2, and
190 RS3) are repeated in a 96-nm interval along the flagellar axoneme in mammalian sperm, sea
191 urchin sperm, *Trypanosoma brucei*, and even in *C. reinhardtii* with stump-like RS3 without a head
192 structure (Fig. 3 A). LRRC23 is a RS protein in chordate axoneme and has been considered
193 especially as the orthologue of RSP15, a RS2 stalk protein in *C. reinhardtii* (Han *et al.*, 2018;
194 Satouh & Inaba, 2009; Yang *et al.*, 2006; Zhang *et al.*, 2021) (Fig 3B). We initially hypothesized
195 the C-terminal truncation of LRRC23 affects the assembly of a RS stalk and/or its incorporation
196 into the RS2. Thus, we tested the protein-protein interaction of normal (hLRRC23^{WT}) and mutant
197 (hLRRC23^{Mut}) human LRRC23 with known RS stalk (RSPH3, RSPH22) or head (RSHP6A,
198 RSHP9) proteins using RSPH-trap assay (Figs 3C-E and EV4A). Purified GST-tagged
199 hLRRC23^{WT} and hLRRC23^{Mut} proteins (Fig 3C and D) were incubated with a recombinant human
200 RSPH enriched by immunoprecipitation (Fig 3E). This trap assay demonstrated that hLRRC23^{WT}
201 interacts only with RSPH9, a RS head protein, among the head and stalk RSPH proteins tested
202 (Figs 3F and EV4B). Interestingly, the previously reported interaction between LRRC23 and
203 RSPH3 (Zhang *et al.*, 2021) is not detected in our assay, which may be due to the different
204 interaction conditions used *in vitro*. Markedly, hLRRC23^{Mut} does not interact with RSPH9,
205 indicating LRRC23 interaction with RS head via its C-terminus. This result also raises the
206 question whether LRRC23 is a head protein of RS, not a stalk protein, a different picture from
207 previous studies. To test this new hypothesis, we performed BLAST search and found *C.*
208 *reinhardtii* RSP15 (Gui *et al.*, 2021) has the highest sequence homology to LRRC34, not LRRC23,
209 in *Ciona intestinalis*. Our phylogenetic and pairwise distance comparison analyses also revealed
210 that LRRC34 orthologs are evolutionarily closer to RSP15 orthologs than LRRC23 orthologs (Figs
211 3G and EV4C). Moreover, AlphaFold-predicted structure of human LRRC34, but not that of
212 LRRC23, presents the same structural features as those of RSP15 (i.e., repeated leucin-rich
213 repeat domains and an α-helix motif in-between) (Fig 3H). *LRRC34* and *LRRC23* share their

214 gene expression patterns among tissues, most abundantly expressed in the tissues known for
215 ciliary and flagellar function such as retina, testis, and fallopian tube (Fig EV4D and E). All these
216 results suggest that LRRC34 is a ciliary and flagellar protein and likely the RSP15 orthologue in
217 chordates, and that LRRC23 function is associated with the RS head.

218

219 **LRRC23 Mutation Disorganizes Radial Spoke 3 in Sperm Flagella**

220 Next, we examined the impact of LRRC23 loss of function by the C-terminal truncation on the
221 subcellular and ultrastructural organization of sperm. We first compared flagellar
222 compartmentalization between *Lrrc23*^{+Δ} and *Lrrc23*^{ΔΔ} sperm. Confocal imaging of
223 immunostained sperm by antibodies against various proteins of known localization did not show
224 any difference on the subflagellar localization of axonemal or peri-axonemal proteins (Fig 4A and
225 EV5A). The levels of such flagellar proteins are also not significantly different between *Lrrc23*^{+Δ}
226 and in *Lrrc23*^{ΔΔ} sperm (Fig EV5B and C). Furthermore, transmission electron microscopy (TEM)
227 did not reveal apparent structural abnormalities in *Lrrc23*^{ΔΔ} sperm flagella (Figs 4B and EV5D).
228 These results indicate overall subflagellar and ultrastructural organization in *Lrrc23*^{ΔΔ} sperm is
229 preserved despite almost complete loss of sperm motility. Any structural abnormality in *Lrrc23*^{ΔΔ}
230 sperm would be subtle and local in the axoneme, likely in the RS head region, which requires a
231 higher resolution microscope technique.

232

233 To determine how the absence of LRRC23 affects sperm structure in more detail, we performed
234 cryo-ET 3D reconstruction to visualize substructural changes of the sperm axoneme (Fig 4C and
235 Movie EV3). The reconstructed tomogram slices revealed striking details of the RS structural
236 difference between WT sperm and *Lrrc23*^{ΔΔ} sperm (Fig 4C). In WT sperm, the three RSs are
237 repeated with a typical pattern, in which RS1 and RS2 are recognized by an additional EM
238 density between them (barrel structure, Leung *et al.*, 2021) followed by RS3 (Fig 4C, left). In
239 *Lrrc23*^{ΔΔ} sperm, EM densities corresponding to RS3 are significantly weaker than those in WT
240 sperm whereas the structural features of RS1 and RS2 are overall kept unaltered from that of WT
241 sperm (Fig 4C, right). These results strongly indicate that the LRRC23 mutation specifically
242 disorganizes RS3 in the sperm axoneme.

243

244 **LRRC23 Is a Head Component of Radial Spoke 3**

245 To visualize the structural defects of RS3 along the *Lrrc23*^{ΔΔ} sperm axoneme in more detail (Fig
246 4C), we performed sub-tomogram averaging (STA) of the axonemal doublets in 96 nm repeat (i.e.,
247 the distance that spans a single set of RS1, RS2, and RS3) on both WT and *Lrrc23*^{ΔΔ}
248 spermatozoa (Figs 5 and EV6). Remarkably, the resulting 3D maps reveal that the head region of
249 RS3 is entirely missing in *Lrrc23*^{ΔΔ} sperm whereas the heads of RS1 and RS2 are intact (Fig 5A
250 and B). In addition, superimposition of the 3D STA maps demonstrates that the junctional
251 structure between RS2 and RS3—present in mouse and human sperm but not in *C. reinhardtii* nor
252 in *T. brucei* flagellar axoneme—is also specifically abolished in *Lrrc23*^{ΔΔ} sperm (Fig 5C). By
253 contrast, *Lrrc23*^{ΔΔ} sperm have intact stalk structures of RS3 like those in WT sperm. Consistent
254 with the protein-protein interaction between LRRC23 and the RS head protein RSPH9 using the
255 RSPH-trap approach (Fig 3), these direct structural observations unarguably clarify that LRRC23
256 is a RS3 head component and the absence of the RS3 head leads to motility defects in *Lrrc23*^{ΔΔ}
257 sperm. These results demonstrate that the C-terminal truncation of LRRC23 prevents the
258 assembly of RS3 head during spermatogenesis, thus preventing functional RS3 complex
259 formation. Taken together, our functional and structural studies using the mouse model
260 recapitulating the human mutation elucidate the molecular pathogenicity of LRRC23 underlying
261 impaired sperm motility and male infertility (Fig 5D).

262

263

264 Discussion

265

266 LRRC23 is a Distinct Head Component of Radial Spoke 3

267 Accumulating evidence on the structural heterogeneity of radial spokes in cilia and flagella
268 suggests that the molecular organization and function of RS3 is distinct from those of RS1 and
269 RS2. For example, the morphology of RS3 head is distinguished from those of RS1 and 2 in
270 mouse motile cilia (Zheng *et al.*, 2021). Moreover, in the tracheal cilia of the PCD patients, RSPH1
271 or RSPH4 loss-of-function mutation specifically abolished RS1 and RS2 heads, but not RS3 head
272 (Lin *et al.*, 2014; Zhao *et al.*, 2021) even though RS3 shares T-shaped structure just like RS1 and
273 RS2 in most eukaryotic motile cilia and flagella (Imhof *et al.*, 2019; Leung *et al.*, 2021; Lin *et al.*,
274 2012; Lin *et al.*, 2014). Despite these findings, the molecular composition of RS3 head remains
275 largely unknown. The current study demonstrates that LRRC23 is a RS3-specific head
276 component. Previous immuno-EM studies showed that LRRC23 is a conserved RS protein in *C.*
277 *intestinalis* and mouse (Pigino *et al.*, 2011; Zhang *et al.*, 2021). It is of note that LRRC23 was
278 originally predicted to be the orthologue of RSP15 in *C. reinhardtii*, a RS2 stalk protein, due to
279 the presence of leucine-rich repeat domains (Gui *et al.*, 2021; Yang *et al.*, 2006). Yet, we found
280 LRRC23 orthologues are not conserved in *C. reinhardtii* in which RS3 is headless and short
281 stump-like, but present in the species where RS3 head structure is preserved, such as *T.*
282 *thermophila*, sea urchin, and mammals. Instead of LRRC23, our phylogenetic and structural
283 comparison strongly suggests that LRRC34 is likely the RSP15 orthologue in chordate animals
284 (Figs 3 and EV4) and a previously unappreciated component of RS2 stalk. Identifying a LRRC34
285 loss-of-function mutation from ciliopathic children further supports that LRRC34 is a RS
286 component (Shamseldin *et al.*, 2020). Our wild type-mutant comparison approach using cryo-ET
287 analyses ultimately clarify that LRRC23 is required for assembling the RS3 head structure (Figs 4
288 and 5), indicating LRRC23 as a RS3 head component. Interestingly, a RS head component,
289 RSPH9, interacts with LRRC23 but the protein level or the localization of RSPH9 is not altered in
290 *Lrrc23*^{ΔΔ} sperm (Fig EV4), suggesting that RSPH9 could be a head component of RS1 and RS2
291 like in *C. reinhardtii* (Gui *et al.*, 2021), but not of RS3. Of note is that an independent study
292 reported that LRRC23 is required for flagellar localization of the RS stalk and fibrous sheath
293 components in mature sperm (Zhang *et al.*, 2021). This discrepancy between two studies is likely
294 due to the presence of the truncated LRRC23 in testis in *Lrrc23*^{ΔΔ} males, which might partly allow
295 flagellar localization of other flagellar components during germ cell development. Although the full
296 picture of molecular composition of RS3 head remains to be revealed, our findings demonstrate
297 LRRC23 is a RS3-specific head component. This conclusion is further supported by the presence
298 of LRRC23 in tracheal cilia (Zhang *et al.*, 2021) that lack the RS2-RS3 bridge structure (Leung *et al.*
299 *et al.*, 2021).

300

301 LRRC23 is required for mammalian sperm-specific bridge structure between RS2 and RS3

302 In motile cilia and flagella, a set of three RSs is repeated along the axoneme (Leung *et al.*, 2021;
303 Lin *et al.*, 2012; Lin *et al.*, 2014; Viswanadha *et al.*, 2017). Notably, a recent cryo-ET study
304 revealed additional RS substructures in mammalian sperm flagella, a barrel structure at RS1 and
305 a junctional bridge structure between RS2 and RS3 (Leung *et al.*, 2021), which were not
306 observed in the sea urchin sperm or human motile cilia (Lin *et al.*, 2014). Furthermore, they are
307 asymmetrically distributed along the mammalian sperm axoneme, corresponding to the peripheral
308 MTDs in a species-specific manner (Chen *et al.*, 2023). Our cryo-ET and STA analyses visualized
309 the mammalian sperm-specific RS1 barrel and RS2-RS3 bridge structures in WT sperm flagella,
310 consistent with Leung *et al.* (Leung *et al.*, 2021). Strikingly, in *Lrrc23* mutant sperm, most of the
311 EM density corresponding to the RS2-RS3 bridge structure is missing and/or altered together with
312 that of the RS3 head (Figs 4 and 5). Considering the absence of RS2-RS3 bridge in tracheal cilia
313 (Lin *et al.*, 2014), LRRC23 also contributes to assemble this flagellar RS substructure. Thus, we
314 speculate that the RS3 and RS2-RS3 bridge structures and their sub-axonemal localization
315 confer non-planar and asymmetric flagellar motility unique to mammalian sperm hyperactivation.
316 As the RS2-RS3 bridge structure is absent in tracheal cilia (Lin *et al.*, 2014), our study
317 unambiguously demonstrates that LRRC23 is required for assembling this bridge structure

318 specifically in mammalian sperm flagella. If so, LRRC23 may be localized at the junction between
319 RS2-RS3 bridge structure and RS3 head. The detailed molecular components that comprise the
320 RS2-RS3 bridge require further study. Profiling and comparing LRRC23 interactomes from
321 mammalian motile cilia and sperm flagella could unveil the cell-type specific molecular
322 organization of RS3.

323

324 **LRRC23 loss of function causes male infertility in mice and human**

325 Loss-of-function mutations in various RS components that are common to motile cilia and sperm
326 flagella were reported to cause PCD and/or male infertility. Loss-of-function mutations of RSPH1
327 (Knowles *et al*, 2014; Kott *et al*, 2013), RSPH3 (Jeanson *et al*, 2015), RSPH4A and RSPH9
328 (Castleman *et al*, 2009) were identified from PCD patients. Some of the male patients carrying
329 RSPH1 and RSPH3 mutations were infertile (Jeanson *et al.*, 2015; Knowles *et al.*, 2014). RSPH1,
330 RSPH4A, and RSPH9 knockout mouse models recapitulated the PCD phenotypes such as
331 hydrocephalus and impaired mucociliary clearance (Yin *et al*, 2019; Yoke *et al*, 2020; Zou *et al*,
332 2020). However, there are other RS components in which mutations only cause male infertility in
333 mice and human. For example, WES of infertile males without PCD symptoms identified
334 mutations in CFAP251 (Auguste *et al*, 2018; Kherraf *et al*, 2018) and CFAP61 (Liu *et al.*, 2021;
335 Ma *et al*, 2021). RSPH6 (Abbasi *et al.*, 2018), CFAP251 (Kherraf *et al.*, 2018), or CFAP61 (Liu *et al.*,
336 2021) deficiency also rendered male mice infertile but without gross abnormalities. These
337 phenotypic differences could be due to a different physiological role of the individual RS
338 component between motile cilia and flagella or a distinct repertoire of the RS components that
339 permits functional redundancy. In our study, LRRC23 mutant mice do not have any apparent
340 gross abnormality but display male infertility (Fig 2). Considering the altered interaction of
341 truncated LRRC23 with RSPH9 *in vitro* (Fig 2), the LRRC23 interaction with RSPH9 is
342 presumably essential for the RS organization and/or sperm motility in mammals. However, since
343 we only examined the interaction of the human proteins, there may be species-specific
344 differences that need to be further investigated. Consistent with our study, a previous study found
345 immotile sperm but normal tracheal ciliary beating in the absence of LRRC23 (Zhang *et al.*,
346 2021). Supportive of these observations, the infertile male patients in the current study do not
347 show PCD symptoms. This phenotype of male infertility without PCD symptoms in both mice and
348 human suggests the mammalian sperm-specific role of LRRC23 in RS structure and function.
349 Physiological implication of LRRC23 and RS3 in motile cilia is unclear but it is likely dispensable
350 for normal ciliary movement probably due to compensatory and/or redundant RS3 proteins
351 specific to cilia. Whether LRRC23 absence would lead to similar structural aberration in RS3
352 head of motile cilia requires further study. Intriguingly, LRRC23 loss-of-function impairs primarily
353 flagellar motility but morphology only marginally, which is distinct from other RS components.
354 For example, the absence of RSPH6, CFAP251, or CFAP61 causes male infertility without PCD
355 symptoms but displays multiple morphological abnormalities of the flagella characterized by
356 absent, short, bent, coiled, and irregular flagella (Toure *et al.*, 2021). By contrast, LRRC23
357 mutation and absence do not cause either PCD nor MMAF phenotypes in human and mouse,
358 suggesting a distinct physiological significance of LRRC23 in reduced sperm motility.

359

360 **Materials and Methods**

361

362 **Subject and family**

363 This study was approved from the review board of Quaid-i-Azam University, Islamabad, Pakistan
364 (IRB00003532, IRB protocol # QAU-171) and the Yale Center for Mendelian Genomics. The
365 family members recruited in this study were explained about the procedure and possible
366 outcomes. The family members provided written consent to attend this study.

367

368 **Sample collection and clinical investigation**

369 **Semen** Semen samples were collected and clinically analyzed according to WHO guidelines
370 (World Health Organization, 2010). Semen samples were collected from the infertile male
371 members after 2-5 days of abstinence from sexual intercourse. The collected semen samples
372 were subjected to the clinical analysis by expert laboratory technologists at Aga Khan Medical
373 Centre (Gilgit, Pakistan) to measure pH, volume, viscosity, and color of the semen and sperm
374 parameters. To assess sperm motility and morphology, the collected semen was liquefied at 37
375 °C for 30-60 minutes. A minimum of 1,000 spermatozoa were counted to analyze sperm motility
376 by the CASA system using an MTG-GmbH analyzer (version 5.4; MTG-MedeaLAB) according to
377 the unit's standard operating procedures based on the WHO guidelines as previously reported
378 (Krause *et al*, 2016; Nawaz *et al*, 2021; Slabbert *et al*, 2015). Sperm from liquified semen were
379 subjected to PAP-staining and the morphology was microscopically analyzed according to the
380 guidelines from WHO and evaluated by a reproductive medicine specialist. PAP-stained sperm
381 were imaged using CMOS camera (Basler acA1300-200µm, Basler AG) equipped in Nikon E200
382 microscope.

383 **Blood** Venous blood samples were collected from attending family members. Collected blood
384 samples were used for karyotyping and genomic DNA extraction. Blood cells cultured with
385 phytohemagglutinin for 72 hours were used for karyotyping. The cultured cells were disrupted and
386 Giemsa-stained. Twenty metaphases were examined to examine karyotypes of each member.
387 Genomic DNA (gDNA) samples were extracted using QIAamp DNA Kit (QIAGEN, Germany).
388 Extracted gDNA samples were subjected to examine microdeletions at the Y-chromosome
389 (AZFa, AZFb, AZFc, and AZFd), whole exome sequencing (WES), and Sanger Sequencing.

390

391 **Whole-Exome Sequencing and Data Analysis**

392 Whole exome sequencing was carried out as described in our previous study (Hwang *et al*,
393 2021b). Briefly, 1.0 µg of genomic DNA from proband's blood is fragmented to an average length
394 of 140 bp using focused acoustic energy (Covaris E210). DNA fragments were subjected to
395 exome capturing using the IDF xGen capture probe panel with an additional "spike-in" of ~2,500
396 region which are total 620 kb of RefGene coding regions. The captured fragments were pair-end
397 sequenced by 101 bp reading using NovaSeq 6000 with S4 flow cell (Illumina). Sequenced reads
398 were aligned to reference human genome (GRCh37/hg19) using the BWA-MEM (Li, 2013) and
399 processed to generate variants using GATK v3.4 (McKenna *et al*, 2010; Van der Auwera *et al*,
400 2013). Variants were annotated with ANNOVAR (Wang *et al*, 2010) and the predicted
401 deleteriousness of non-synonymous variants was determined by MetaSVM (Dong *et al*, 2015).
402 Either loss of function mutations of stop-gains, stop-losses, frameshift indels, and canonical
403 splice-sites or deleterious missense mutations predicted by MetaSVM were considered to
404 potentially damaging. Recessive variants of which MAF values in Genome Aggregation Database
405 (gnomeAD), v2.1 (Lek *et al*, 2016; <https://gnomad.broadinstitute.org/>) are lower than 10⁻³ were
406 considered for rare variants. Rare damaging variants were further filtered to exclude false-

407 positives using the follow criteria: (1) PASS for GATK variant quality score recalibration, (2) MAF
408 $\leq 2.0 \times 10^{-5}$ in the gnomAD, (3) DP ≥ 8 independent reads, (4) GC score ≥ 20 , (5) MQ score ≥ 40 ,
409 (6) PLdiff/DP ≥ 8 , and (7) indels in Low Complexity Regions. Co-segregation of candidate
410 variants with the phenotypes were confirmed by genomic DNA PCR and Sanger sequencing.
411 Genomic DNA PCR was performed with using OneTaq[®] 2X Master Mix (NEB) and used primer
412 pairs were; Fwd: 5'-GCTGAGCATTGGAGTGGC-3' and Rev: 5'-
413 CCTGCTAGGTGGCTGTGTAT-3' for *LRRC23*, Fwd: 5'-TGAACCCCTGGCACAAC-3' and Rev:
414 5'-TTTTTACTCAGCGATACCACATTCACAG-3' for *SCN5A*, Fwd: 5'-
415 TGGCTAAATCCCATCCAGTCC-3' and Rev: 5'-GAGTCTGTCCTTGCCCGTAG-3' for *NOX1*,
416 and Fwd: 5'-GATTGTCATCGCCTTGTTTCATC-3' and Rev: 5'-TGTTTTGTGGTGGCACAGTC-3'
417 for *PRRG3*. Amplified PCR products were subjected to Sanger sequencing.

418

419 **Kinship Analysis**

420 Kinship coefficient was estimated to confirm pedigree information and pairwise relatedness of
421 proband using KING v2.2.4 (Manichaikul *et al*, 2010). Inbreeding coefficient was calculated by
422 homozygosity-by-descent (HBD). HBD segment in the proband was detected by Beagle v3.3.2
423 (Browning & Browning, 2011). Homozygosity in segments over 2 cM was considered for
424 consanguinity.

425

426 **Animals**

427 Wildtype C57BL/6 mice were from Charles River Laboratory. Mice were cared in accordance with
428 the guidelines approved by Institutional Animal Care and Use Committee (IACUC) for Yale
429 University (#20079).

430

431 **Generation of the *Lrrc23*-mutant mice and genotyping**

432 *Lrrc23*-mutant mice were generated on C57BL/6 background using CRISPR/Cas9 genome
433 editing as described (Chen *et al*, 2016; Yang *et al*, 2014). Two guide RNAs targeting the 5th (5'-
434 CATATGGTAACATTGACCCAGGG-3') and 7th (5'-CGTCTCTACCAGCTATACAGCGG-3') were
435 *in vitro* transcribed and purified. The sgRNAs/Cas9 RNPs were complexed and electroporated
436 into zygotes from C57BL/6J. The embryos were transplanted to oviducts of pseudopregnant CD-1
437 foster females and founders' toe were biopsied to extract gDNA. Truncation of the target region
438 was confirmed by gDNA PCR with F3 (5'-CACTTTTCCTGCCTCTGTGTCC-3') and R3 (5'-
439 AGCATCTCCCACTTCCTGTGAC-3') primers. The amplicons were Sanger sequenced and
440 founder females with 4126bp or 4128bp truncation at the genomic region (*4126del* and *4135del*)
441 were mated with C57BL/6 WT mice to confirm the germline transmission of the alleles. Two
442 mutant mice lines were maintained and genotyped with F3-R3 pairs for the mutant allele and F2
443 (5'-TTGTGGTGGTGGGGAGATAG-3')-R2 (5'-GTGGTGATGGACGGGTGT-3') pair for WT allele.

444

445 **Mouse sperm preparation**

446 Sperm were collected from cauda epididymis of the adult mice by swim-out in M2 medium (EMD
447 Millipore). To induce capacitation, the epididymal sperm were incubated in human tubular fluid
448 (HTF; EMD Millipore) at 2.0×10^6 cells/ml concentration for 90 minutes at 37 °C, 5% CO₂
449 condition.

450

451 **Mammalian Cell culture and transient protein expression**

452 Human embryonic kidney 293T cells (ATTC) were cultured in DMEM (Gibco) supplemented with
453 10% FBS (Gibco) and 1X Pen/Strep (Gibco) at 37 °C, 5% CO₂ condition. Cultured cells were

454 transfected with Lipofectamine 2000 (Invitrogen) or polyethylenimine (PEI) to express
455 recombinant protein transiently. Transfected cells were used for co-immunoprecipitation or
456 modified trap-assay.

457

458 **RNA extraction, cDNA synthesis, and PCR**

459 Total RNA was extracted from transfected 293T cells and frozen mouse testes using RNeasy
460 Mini kit (QIAGEN). Extracted RNA was used for cDNA synthesis using iScript cDNA Synthesis kit
461 (BIO-RAD) in accordance with manufacturer's instruction. Synthesized testis cDNAs were used
462 for endpoint PCR or quantitative PCR using OneTaq 2X Master Mix (NEB) or with iTaq Universal
463 SYBR Green Supermix (BIO-RAD), respectively. Primer pairs, F1 (5'-
464 GGCATCTCTCATCCTCGTCT-3') - R1 (5'-AGCCACTCAGGGTGTCAATC-3'), F4 (5'-
465 TTGGCGTCTCAGCACAAAG-3') - R4 (5'-CTCGAAGCTCCAGGGTGT-3'), and F5 (5'-
466 CTGGACCCCGAGAGACTG-3') - R5 (5'-AGTTTTACCCCGACCTGTG-3') were used for
467 endpoint PCR; E3 (5'-AGCTGGAGGCTAAGGACAGG-3') - E4 (5'-
468 GAGCGGCGATATGTCTGTAA-3') and E7 (5'-GTCAGAGGCTGAAGGAGGAA-3') - E8 (5'-
469 TATCAGTTCTTGGGGCCAGT-3') were used for quantitative PCR. TBP was used to calculate
470 relative transcript levels in mouse testes by $\Delta\Delta C_t$ method.

471

472 **Antibodies and reagent**

473 Rabbit polyclonal RSPH3B were described in previous studies (Hwang *et al.*, 2021b). Rabbit
474 polyclonal anti-LRRC23 (α -118, PA5-63449; α -208, PA5-58095), DNAH1 (PA5-57826), DNAH2
475 (PA5-64309), and DNAH9 (PA5-45744) were from Invitrogen. Rabbit polyclonal SEPTIN4 (NBP1-
476 90093) antibody was from Novus Biologicals. Mouse monoclonal anti-His-tag (66005-1-Ig) and
477 rabbit polyclonal anti-AKAP3 (13907-1-AP), RSPH9 (23253-1-AP), and RSPH22 (16811-1-AP)
478 were purchased from Proteintech. Rabbit polyclonal TOM20 (sc-11415) was from SantaCruz.
479 Mouse monoclonal anti-acetylated tubulin (AcTub, clone 6-11B-1, 7451), CALM1 (05-173), pTyr
480 (clone 4G10, 05-321), and HA (clone HA-7, H3663) and rabbit polyclonal anti-SEPTIN12
481 (HPA041128) were from Sigma-Aldrich. Rabbit and mouse monoclonal anti-DYKDDDDK (clone
482 D6W5B, 86861; clone 9A3, 8146) were from Cell Signaling Technology. Rabbit polyclonal ODF2
483 and AKAP4 were gifted from Dr. Edward M. Eddy. Rabbit anti-RSPH6A sera was gifted from Dr.
484 Masahito Ikawa. HRP-conjugated goat anti-mouse and anti-rabbit IgG were from Jackson
485 ImmunoResearch. Goat anti-rabbit IgG conjugated with Alexa 568, Lectin PNA conjugated with
486 Alexa 647, and Hoechst dye were from Invitrogen.

487

488 **Protein extraction, solubilization, and immunoblotting**

489 **Testis** Adult mouse testes were homogenized in 0.32M using dounce homogenizer followed by
490 centrifugation for 15 minutes at 4 °C, 1000 x g to pellet nucleus and debris. Supernatants was
491 collected and centrifuged at 4 °C, 100,000 rpm for an hour to separate cytosolic and microsome
492 fractions. Volume-equivalent cytosolic and microsome fractions were lysed with 2X LDS
493 sampling buffer and denatured by boiling at 75 °C with 50 mM dithiothreitol (DTT) for 2 or 10
494 minutes, respectively, for SDS-PAGE and immunoblotting. Primary antibodies used for
495 immunoblotting were: rabbit polyclonal anti-LRRC23 (α -118 and α -208, both 1:500) and mouse
496 monoclonal anti-AcTub (1:2,000), and calmodulin (1:1,000).

497 **Epididymal sperm** Collected epididymal cells were washed with PBS and lysed using 2X
498 LDS by vortexing at room temperature (RT) for 10 minutes to extract whole sperm proteins as
499 described previously (Hwang *et al.*, 2022). The lysates were centrifuged for 10 minutes at 4 °C,
500 18,000 x g and the supernatant were mixed to 50 mM DTT followed by boiling at 75 °C for 10

501 minutes for denaturation. The samples were subjected to SDS-PAGE and immunoblotting. The
502 used primary antibodies were: rabbit polyclonal anti-LRRC23 (α -118 and α -208, 1:500), AKAP3
503 (1:2,000), RSPH9 (1:500), RSPH22 (1:1,000), ODF2 (1:2,000), AKAP4 (1:2,000), and RSPH3
504 (1:500), rabbit anti-RSPH6A sera (1:500), and mouse monoclonal AcTub (1:20,000).

505 **293T cells** 293T cells were lysed using 0.5% Triton X-100 in 10 mM HEPES, 140 mM NaCl,
506 pH7.4 buffer (1X HEPES buffer) for 2 hours at 4 °C with gentle rocking. The lysates were
507 centrifuged at 4 °C, 18,000 x g for 30 minutes. Supernatant with solubilized proteins were used
508 for protein interaction tests or mixed to 1X LDS and 50 mM DTT followed by boiling at 75 °C for 2
509 minutes. Denatured samples were used for immunoblotting. Mouse monoclonal anti-HA (1:4000)
510 and FLAG (1:1000), and rabbit monoclonal anti-FLAG (1:1000) were used for primary antibody.
511 HRP-conjugated goat anti-rabbit and goat anti-mouse IgG were used for secondary antibodies
512 (0.1 μ g/ml). SuperSignal™ Western Blot Enhancer (Thermo Scientific) was used for testis and
513 sperm immunoblotting with anti-LRRC23 antibody (α -118).

514

515 **Molecular cloning**

516 Human *LRRC23* ORF clone (HG24717-UT, SinoBiological) and the partial region of the human
517 *LRRC23* 5th intron amplified by PCR was subcloned into phCMV3 vector to generate mammalian
518 expression constructs for human *LRRC23* (*phCMV3-FLAG-hLRRC23^{ORF}-HA*, *phCMV3-FLAG-*
519 *hLRRC23^{WT}-HA*, and *phCMV3-FLAG-hLRRC23^{Mut}-HA*). cDNA clones of human *RSPH3* (616166,
520 Horizon Discovery), *RSPH6A* (5270908, Horizon Discovery), *RSPH9* (5296237, Horizon
521 Discovery), and *RSPH22* (OHu31347, GenScript) was subcloned into *phCMV3* to express human
522 RSPH proteins tagged with FLAG at C-termini. A stop codon was placed at the upstream of
523 sequences encoding HA in *phCMV3* vector for tagging FLAG at C-termini. ORFs encoding full-
524 length and the predicted mutant LRRC23 were amplified from *phCMV3-FLAG-hLRRC23^{ORF}-HA*
525 constructs and subcloned into *pGEX-6P2* vector to generate *pGEX-6P2-hLRRC23^{WT}* and *pGEX-*
526 *6P2-hLRRC23^{Mut}* constructs tagging with HA at C-termini. ORFs for each construct were
527 amplified using Q5 Hot Start High-Fidelity 2X Master Mix (NEB) and subcloned into linear vectors
528 using NEBuilder HiFi DNA Assembly Kit (NEB)

529

530 **Recombinant protein purification**

531 Bacterial expression constructs were transformed to BL21-CodonPlus(DE3)-RIL competent cells
532 (Agilent Technologies). Fresh colonies were cultured into LB with antibiotics overnight at 37 °C
533 and cultured further after 50 times dilution at 37 °C until OD₆₀₀ values reach to 0.5-0.8. The
534 cultivates were treated with 1mM IPTG to express recombinant proteins and cultured further for
535 16-18 hours at 16 °C. IPTG-treated bacteria were washed with PBS and eluted with 1X HEPES
536 buffer containing 1% Triton X-100 and EDTA-free protease inhibitor cocktail (Roche) The elutes
537 were sonicated and centrifuged at 18,000 x g, 4 °C for 1 hour. Supernatant were collected and
538 incubated with glutathione agarose (Pierce) for overnight at 4 C to purify recombinant GST and
539 GST-tagged human LRRC23^{WT} and LRRC23^{Mut}. The incubated resins were washed with PBS
540 and eluted with 1X HEPES buffer supplemented with 10 mM reduced glutathione. The elutes
541 were dialyzed against 1X HEPES buffer with 50% glycerol for overnight at 4 °C. Purified proteins
542 were subjected to Coomassie gel staining using Imperial™ Protein Stain (Thermo Scientific) and
543 immunoblotting.

544

545 **Modified trap assay**

546 293T cells to express FLAG-tagged human RSPH proteins transiently were lysed with 1% Triton
547 X-100 in 1X HEPES buffer with EDTA-free protease inhibitor cocktail (Roche) by rocking at 4 °C

548 for 2 hours. The lysates were centrifuged at 18,000 x g for 30 minutes at 4 °C and the
549 supernatant was incubated with Surebeads™ Protein A Magnetic Bead (Bio-rad) conjugated with
550 rabbit monoclonal DYKDDDDK antibody at RT for two hours. The magnetic beads were washed
551 with 1% Triton X-100 in 1X HEPES buffer two times and 0.2% Triton X-100 in 1X HEPES buffer.
552 Purified GST, GST-tagged human LRRC23^{WT} and LRRC23^{Mut} proteins were incubated with the
553 washed magnetic beads in 0.2% Triton X-100 in 1X HEPES buffer at 4 °C for overnight.
554 Incubated magnetic beads were washed with 0.2% Triton X-100 in 1X HEPES buffer for three
555 times and eluted with 2X LDS buffer containing 50 mM DTT followed by denatured 75 °C for 10
556 minutes.

557

558 **Sperm fluorescence staining**

559 Epididymal sperm cells were washed with PBS and attached on the glass coverslips by
560 centrifugation at 700 x g for 5 minutes. The coverslips were fixed with either 4% PFA in PBS at
561 RT for 10 minutes (SEPTIN4, SEPTIN12, RSPH3, DNAH2, DNAH9, TOM20, and LRRC23) or
562 acetone at - 20 °C for 5 minutes (RSPH9, DNAH1, AKAP4, ODF2, and AcTub). PFA fixed
563 coverslips were washed with PBS three times and permeablized with 0.1% (SEPTIN4 and
564 SEPTIN12), 0.5% (RSPH3, LRRC23, and DNAH9), or 1% (DNAH2) Triton X-100 in PBS at RT
565 for 10 minutes. Acetone-fixed coverslips were rehydrated by washing with 0.1% Triton X-100 in
566 PBS and PBS. Permeablized coverslips were blocked with 10 % normal goat serum in PBS and
567 incubated with primary antibodies in blocking buffer at 4 °C overnight. Used primary antibodies
568 were: Rabbit polyclonal anti-LRRC23 (α -118, 1:100), SEPTIN4 (1 μ g/ml), SEPTIN12 (1:100),
569 RSPH3 (10 μ g/ml), RSPH9 (1:100), DNAH1 (3 μ g/ml), DNAH2 (0.5 μ g/ml), DNAH9 (5 μ g/ml),
570 TOM20 (1:50), AKAP4 (1:100), and ODF2 (1:50), and mouse monoclonal anti-AcTub (1:200).
571 Coverslips were washed with 0.1% Triton X-100 in PBS one time and PBS two times and
572 incubated with either goat anti-rabbit or mouse IgG conjugated with Alexa 568 in blocking buffer
573 at RT for an hour. The coverslips were washed with PBS three times and mounted on the glass
574 slide using Vectasheild (Vector Laboratory). To observe sperm acrosome, PFA-fixed coverslips
575 were incubated with PNA conjugated with Alexa 647 at RT for an hour. Fluorescence stained
576 coverslips were imaged using Zeiss LSM710 Elyra P1 with Plan-Apochromat 63X/1.40 objective
577 (Carl Zeiss). Hoechst were used for counter staining.

578

579 **Mating test**

580 Adult heterozygous and homozygous *Lrrc23* mutant male mice were housed with adult female
581 mice with normal fertility and monitored over two months. The pregnancy and litter size were
582 recorded.

583

584 **Sperm motility analysis**

585 **Computer-assisted sperm analysis** Computer-assisted sperm analysis (CASA) was
586 performed as previous study (Hwang *et al*, 2022). Briefly, sperm cells at 3.0×10^6 cells/ml
587 concentration were loaded in slide chamber (CellVizion) and their motility parameters were
588 measured on 37 °C warm-stage. Motility of over 200 sperm was recorded using CMOS video
589 camera (Basler acA1300-200 μ m, Basler AG) at 50 frame per seconds (fps) through 10x phase
590 contrast objective (CFI Plan Achrom 10X/0.25 Ph1 BM, Nikon) equipped in Nikon E200
591 microscope. The recorded sperm motility was analyzed using Sperm Class Analyzer software
592 (Microptic).

593 **Sperm swimming path analysis** Sperm free swimming analysis was conducted as
594 previous study (Hwang *et al*, 2019; Hwang *et al*, 2021a). Briefly, sperm cells were transferred to

595 Delta-T culture dish controller (Biotech) filled with 37 °C HEPES-buffered HTF medium with
596 0.3% methylcellulose (Chung *et al*, 2017). Sperm swimming was imaged using pco.edge sCMOS
597 camera in Axio observer Z1 microscope (Carl Zeiss) for 2 seconds with 100 fps. FIJI software
598 (Schindelin *et al*, 2012) was used to generate overlaid images to show sperm swimming paths.

599 **Flagellar waveform analysis** To analyze sperm flagellar waveform, 2.0×10^5 cells of
600 capacitated and non-capacitated sperm cells were placed into 37 °C HEPES-buffered HTF
601 medium (Chung *et al*, 2017) in fibronectin-coated Delta-T culture dish controller (Biotech).
602 Flagellar movement of the head-tethered sperm was recorded using pco.edge sCMOS camera
603 equipped in Axio observer Z1 microscope (Carl Zeiss) for 2 seconds with 200 fps. Recorded
604 image stacks were applied to generate overlaid images to show flagellar waveform for two
605 beating cycles with FIJI software (Schindelin *et al*, 2012).

606

607 **Sequence alignment and phylogenetic analysis**

608 Amino acid sequences of human and mouse normal and mutant LRRC23 were aligned using
609 Clustal Omega (<https://www.ebi.ac.uk/Tools/msa/clustalo/>). Amino acids sequences of LRRC23
610 and LRRC34 orthologs and *Chlamydomonas reinhardtii* RSP15 were aligned with ClustalW for
611 phylogenetic analysis using MEGA7 (Kumar *et al*, 2016). Pairwise distances between the
612 sequences were calculated with default option. An unrooted phylogenetic tree was generated by
613 maximum-likelihood analysis with 500 bootstrap replications.

614

615 **Protein structure analysis**

616 Radial spoke 2 and RSP15 structures of the *C. reinhardtii* were from RCSC Protein Data Bank,
617 PDB (<https://www.rcsb.org/>; 7JU4). Predicted structures of human LRRC23 (Q53EV4) and
618 LRRC34 (Q8IZ02) were from AlphaFold Protein Structure Database (Jumper *et al*, 2021;
619 <https://alphafold.ebi.ac.uk/>). Protein structures were rendered and visualized by Mol* 3D Viewer
620 at RCSC PDB.

621

622 **Tissue and testicular expression analysis**

623 Transcript expression data of *LRRC23* and *LRRC34* in human tissues was obtained from GTEx
624 and is based on The Human Protein Atlas version 21.0 and Ensembl version 103.38
625 (<https://www.proteinatlas.org/about/download>). Medians of the normalized transcript per million
626 (nTPM) are used to calculate relative tissue expression levels. Relative tissue expression levels
627 of *LRRC23* and *LRRC34* are represented as heatmap using GraphPad Prism 8.0 (GraphPad
628 Software Inc., San Diego, CA). UMAP images for the single-cell expression of *LRRC23* and
629 *LRRC34* in human testis are obtained from UCSC Cell browser (Soraggi *et al*, 2021;
630 <https://cells.ucsc.edu/?ds=testis>).

631

632 **Transmission electron microscopy**

633 Transmission electron microscopy was performed as previous study (Hwang *et al*, 2021b).
634 Washed epididymal sperm were pelleted by centrifugation and fixed with 2.5% glutaraldehyde
635 and 2% paraformaldehyde in 0.1M cacodylate buffer pH7.0 for 30 minutes at RT and for 1 hour at
636 4 °C. The fixed pellets were briefly washed with 0.1M cacodylate buffer pH7.0 and placed in 2%
637 agar. The chilled blocks were trimmed and rinsed with 0.1M cacodylate buffer followed by placed
638 in 0.1% tannic acid in 0.1M cacodylate buffer for 1 hour. The samples were washed and post-
639 fixed in 1% osmium tetroxide and 0.15% potassium ferrocyanide in 0.1M cacodylate buffer for 1
640 hour. Post-fixed samples were rinsed with the cacodylate buffer and distilled water and subjected
641 to en bloc staining in 2% aqueous uranyl acetate for 1 hour. The samples were dehydrated with

642 ethanol series and infiltrated with epoxy resin Embed 812 (Electron Microscopy Sciences). The
643 resins were placed in silicone molds and backed for 24 hours at 60 °C. The blocks were
644 sectioned in 60 nm depth using Leica UltraCut UC7 and the sections were collected on the
645 formvar/carbon-coated grids. Sections on the grids were stained using 2% uranyl acetate and
646 lead citrate. The stained grids were imaged using MORADA CCD camera (Olympus) equipped in
647 FEI Tecnai Biotwin Transmission Electron Microscope (FEI, Hillsboro, OR) at 80 KV.

648

649 **Cryo-electron tomography**

650 **Grid preparation** Grids for sample imaging were prepared as a previously report (Leung *et*
651 *al.*, 2021). The Quantifoil R2/2 gold grids were glow discharged for 30 seconds at 15mA and $1.5 \times$
652 10^5 cells of WT or *Lrrc23*^{ΔΔ} sperm were loaded on the grids followed by incubation at RT for 1
653 minutes. The grids were blotted manually from the back site for ~4 seconds using a manual
654 plunger freezer and immediately plunged into liquid ethane and stored in liquid nitrogen.

655 **Cryo-ET data collection** Prepared grids with proper ice particles were screened using a
656 Glacios microscope (200 KV, ThermoFisher Scientific) at the Yale Science Hill Electron
657 Microscopy Facility. The screened grids were transferred to the Titan Krios microscope (300 KV,
658 ThermoFisher Scientific) equipped with a Bioquantum Energy Filter and a K3 direct electron
659 detector (Gatan) for data collection at the Yale West Campus Electron Microscopy Facility. Data
660 was collected automatically using SerialEM (Mastrorarde, 2005). All images were recorded under
661 super-resolution mode with the physical pixel size 3.4 Å (1.7 Å for super resolution movies). 20
662 and 60 tilt series of WT and *Lrrc23*^{ΔΔ} mouse sperm were collected with the Volta phase plate at a
663 target defocus around -1 μm. Grouped dose-symmetric scheme spanning from -51° to 51° at 3°
664 increment was applied for tilt series acquisition, with a total dose at 100e-/Å².

665 **Tomogram reconstruction** Process of tomogram reconstruction was streamlined using in-
666 house scripts. The movie frames were aligned first using MotionCorr2 and the micrographs were
667 binned with a factor two (Zheng *et al.*, 2016). Tilt series stack was generated using in-house
668 script. The tilt-series was aligned by AreTomo 1.0.6 (Zheng *et al.*, 2022) to generate XF files
669 which are comparable for IMOD (Kremer *et al.*, 1996). The initial CTF parameters were estimated
670 using Ctfind4 (Rohou & Grigorieff, 2015). The tomograms were then reconstructed with a binning
671 factor six with 20.4 Å pixel size by IMOD with SIRT algorithm for visualization, particle picking and
672 initial sub-tomogram averaging.

673

674 **Sub-Tomogram Averaging of 96-nm axonemal doublet repeat**

675 **Initial alignment using PEET** MTDs were manually traced in IMOD (Kremer *et al.*, 1996). After
676 manual tracing, a polynomial function with degree five was fitted to each microtubule doublet with
677 24 nm of a sampling distance (Fig EV6C). The polarity of each tomogram is manually determined
678 to reduce the error during subsequent alignment. The 24-nm repeat particles were first aligned
679 using PEET Version 1.15.0 under “Particle model points” and “align particle Y axes” options
680 (Heumann *et al.*, 2011; Nicastro *et al.*, 2006). A published map of 96-nm MTD repeat in WT
681 mouse sperm (EMD-12133; Leung *et al.*, 2021) was low-pass filtered to 60 Å and used as the
682 initial reference. A mask covering two adjacent MTDs was generated with 160 x 160 x 160 nm³
683 dimension of sub-tomogram particle. Only “Phi” angle and translational shifts were searched
684 during the alignment. After the initial alignment, positions of the particles were placed at center
685 based on the translational shifts. The Euler angles were extracted and transformed to RELION
686 Euler angle convention (ZYZ) using the MOTL2Relion command in PEET. In-house script was
687 used to gather the coordinates and corresponding Euler angle information for subsequent
688 RELION4 sub-tomogram averaging analysis.

689 **Refinement and classification** After the metadata preparation, the sub-tomogram particles were
690 made in RELION4 (Zivanov *et al*, 2022) with the binning factor of six. Local 3D refinement with a
691 mask covering one 96-nm MTD was performed. After refinement, the features of 24-nm repeat of
692 outer dynein arm was observed (Fig EV6D). A smaller mask only covering the inner dynein arm
693 and radial spoke was created for the focused classification without alignment (Fig EV6E). After
694 classification, equivalent 96-nm MTD repeat classes were separated (Fig EV6E). One of the
695 classes was selected for the future process. New sub-tomogram particles with binning factor
696 three and corresponding 10.2 Å of pixel size were generated. Another local refinement was
697 performed with a 96-nm MTD mask. Resolution was estimated using the Fourier shell correlation
698 (FSC) at a cut-off of 0.143 in RELION4 (Zivanov *et al.*, 2022). Details of acquisition parameters
699 and particle numbers are summarized in Table EV3.

700 **Visualization** Images for cryo-ET and sub-tomogram averaging were rendered using IMOD
701 (Kremer *et al.*, 1996) and UCSF ChimeraX (Goddard *et al*, 2018).

702

703 **Statistical analysis**

704 Statistical analyses were performed using Student's t-test or Mann-Whitney U test. Significant
705 differences were considered at * $p \leq 0.05$, ** $p < 0.01$, and *** $p < 0.001$.

706

707 **Data availability**

708 The structures for radial spokes from WT (EMD-29013) and *LRRC23^{Δ/Δ}* (EMD-28606) sperm
709 resolved by cryo-ET and STA are deposited to Electron Microscopy Data Bank
710 (<https://ebi.ac.uk/pdbe/emdb>).

711

712 **Acknowledgments**

713 The authors highly appreciate participation of the family members in the study presented here.
714 We also thank Muhammad Umair, Khadim Shah, Imran Ullah, Hammal Khan for their help to visit
715 the family for interviews and participation in clinical assessment, Habibur Rehmen and Rina Raza
716 from Aga Khan Medical Centre for clinical semen analyses, Jong-Nam Oh for preparing samples
717 for WES, Case Porter and Miriam Hill for their help in PCR and Sanger sequencing, the Yale
718 Center for Cellular and Molecular Imaging for assistance in transmission electron microscopy, Dr.
719 Masahito Ikawa from Osaka University for sharing anti-RSPH6A sera. This study was supported
720 by start-up funds from Yale University School of Medicine and National Institute of Child Health
721 and Human Development (R01HD096745) to J-JC; start-up funds from Yale University, National
722 Institute of General Medical Sciences (R35GM142959) to KZ; Pakistan Academy of Sciences
723 (PAS-171) to WA; National Human Genome Research Institute (UM1HG006504) to the Yale
724 Center for Mendelian Genomics. JH was in part supported by Postdoctoral Fellowship from MCI.
725 SN was supported by Pakistan Higher Education Commission International Research Support
726 Initiative Program. JC was in part supported by a Korea University Medical Center Grant. The
727 Genome Sequencing Program Coordinating Center (U24 HG008956) contributed to cross-
728 program scientific initiatives and provided logistical and general study coordination.

729

730 **Author Contributions**

731 **Jae Yeon Hwang:** Conceptualization; methodology; formal analysis; data curation; writing -
732 original draft; writing – review and editing. **Pengxin Chai:** Methodology; formal analysis; data
733 curation; writing – original draft. **Shoaib Nawaz:** Investigation; methodology; formal analysis.
734 **Jungmin Choi:** Methodology; formal analysis; data curation. **Francesc Lopez-Giraldez:**
735 Methodology; formal analysis; data curation. **Shabir Hussain:** Investigation. **Kaya Bilguvar;**
736 Formal analysis. **Shrikant Mane:** Formal analysis. **Richard P. Lifton;** Resource. **Wasim**
737 **Ahmad:** Resource. **Kai Zhang:** Conceptualization; formal analysis; writing – review and editing;
738 resource; funding acquisition. **Jean-Ju Chung:** Conceptualization; formal analysis; data curation;
739 writing - original draft; writing – review and editing; resource; supervision; funding acquisition.

740

741 **Disclosure and competing interests statement**

742 The authors declare that they have no conflict of interest.

743

744

745 References

- 746 Abbasi F, Miyata H, Shimada K, Morohoshi A, Nozawa K, Matsumura T, Xu Z, Pratiwi P, Ikawa M
747 (2018) RSPH6A is required for sperm flagellum formation and male fertility in mice. *J Cell Sci* 131
748 Auguste Y, Delague V, Desvignes JP, Longepied G, Gnisci A, Besnier P, Levy N, Beroud C,
749 Megarbane A, Metzler-Guillemain C *et al* (2018) Loss of Calmodulin- and Radial-Spoke-
750 Associated Complex Protein CFAP251 Leads to Immotile Spermatozoa Lacking Mitochondria and
751 Infertility in Men. *Am J Hum Genet* 103: 413-420
- 752 Bazan R, Schrofel A, Joachimiak E, Poprzeczko M, Pigino G, Wloga D (2021) Ccdc113/Ccdc96
753 complex, a novel regulator of ciliary beating that connects radial spoke 3 to dynein g and the
754 nexin link. *PLoS Genet* 17: e1009388
- 755 Browning BL, Browning SR (2011) A fast, powerful method for detecting identity by descent. *The*
756 *American Journal of Human Genetics* 88: 173-182
- 757 Castleman VH, Romio L, Chodhari R, Hirst RA, de Castro SC, Parker KA, Ybot-Gonzalez P, Emes
758 RD, Wilson SW, Wallis C *et al* (2009) Mutations in radial spoke head protein genes RSPH9 and
759 RSPH4A cause primary ciliary dyskinesia with central-microtubular-pair abnormalities. *Am J Hum*
760 *Genet* 84: 197-209
- 761 Cavarocchi E, Whitfield M, Saez F, Toure A (2022) Sperm Ion Transporters and Channels in
762 Human Asthenozoospermia: Genetic Etiology, Lessons from Animal Models, and Clinical
763 Perspectives. *Int J Mol Sci* 23
- 764 Chen S, Lee B, Lee AY-F, Modzelewski AJ, He L (2016) Highly efficient mouse genome editing by
765 CRISPR ribonucleoprotein electroporation of zygotes. *Journal of Biological Chemistry* 291:
766 14457-14467
- 767 Chen Z, Greenan GA, Shiozaki M, Liu Y, Skinner WM, Zhao X, Zhao S, Yan R, Yu Z, Lishko PV *et al*
768 (2023) In situ cryo-electron tomography reveals the asymmetric architecture of mammalian
769 sperm axonemes. *Nat Struct Mol Biol* 30: 360-369
- 770 Chung JJ, Miki K, Kim D, Shim SH, Shi HF, Hwang JY, Cai X, Iseri Y, Zhuang X, Clapham DE (2017)
771 CatSperzeta regulates the structural continuity of sperm Ca(2+) signaling domains and is
772 required for normal fertility. *Elife* 6
- 773 Curi SM, Ariagno JI, Chenlo PH, Mendeluk GR, Pugliese MN, Sardi Segovia LM, Repetto HE,
774 Blanco AM (2003) Asthenozoospermia: analysis of a large population. *Arch Androl* 49: 343-349
- 775 Dong C, Wei P, Jian X, Gibbs R, Boerwinkle E, Wang K, Liu X (2015) Comparison and integration
776 of deleteriousness prediction methods for nonsynonymous SNVs in whole exome sequencing
777 studies. *Human molecular genetics* 24: 2125-2137
- 778 Goddard TD, Huang CC, Meng EC, Pettersen EF, Couch GS, Morris JH, Ferrin TE (2018) UCSF
779 ChimeraX: Meeting modern challenges in visualization and analysis. *Protein Sci* 27: 14-25
- 780 Gui M, Ma M, Sze-Tu E, Wang X, Koh F, Zhong ED, Berger B, Davis JH, Dutcher SK, Zhang R *et al*
781 (2021) Structures of radial spokes and associated complexes important for ciliary motility. *Nat*
782 *Struct Mol Biol* 28: 29-37
- 783 Han X, Xie H, Wang Y, Zhao C (2018) Radial spoke proteins regulate otolith formation during
784 early zebrafish development. *FASEB J* 32: 3984-3992
- 785 Heumann JM, Hoenger A, Mastronarde DN (2011) Clustering and variance maps for cryo-
786 electron tomography using wedge-masked differences. *J Struct Biol* 175: 288-299
- 787 Hwang JY, Mallowetz N, Zhang Y, Everley RA, Gygi SP, Bewersdorf J, Lishko PV, Chung JJ (2019)
788 Dual Sensing of Physiologic pH and Calcium by EFCAB9 Regulates Sperm Motility. *Cell* 177: 1480-
789 1494 e1419

790 Hwang JY, Maziarz J, Wagner GP, Chung JJ (2021a) Molecular Evolution of CatSper in Mammals
791 and Function of Sperm Hyperactivation in Gray Short-Tailed Opossum. *Cells* 10
792 Hwang JY, Nawaz S, Choi J, Wang H, Hussain S, Nawaz M, Lopez-Giraldez F, Jeong K, Dong W, Oh
793 JN *et al* (2021b) Genetic Defects in DNAH2 Underlie Male Infertility With Multiple Morphological
794 Abnormalities of the Sperm Flagella in Humans and Mice. *Front Cell Dev Biol* 9: 662903
795 Hwang JY, Wang H, Lu Y, Ikawa M, Chung JJ (2022) C2cd6-encoded CatSpertau targets sperm
796 calcium channel to Ca(2+) signaling domains in the flagellar membrane. *Cell Rep* 38: 110226
797 Imhof S, Zhang J, Wang H, Bui KH, Nguyen H, Atanasov I, Hui WH, Yang SK, Zhou ZH, Hill KL
798 (2019) Cryo electron tomography with volta phase plate reveals novel structural foundations of
799 the 96-nm axonemal repeat in the pathogen *Trypanosoma brucei*. *Elife* 8
800 Inaba K (2011) Sperm flagella: comparative and phylogenetic perspectives of protein
801 components. *Mol Hum Reprod* 17: 524-538
802 Ishikawa T (2017) Axoneme Structure from Motile Cilia. *Cold Spring Harb Perspect Biol* 9
803 Jeanson L, Copin B, Papon JF, Dastot-Le Moal F, Duquesnoy P, Montantin G, Cadranet J, Corvol H,
804 Coste A, Desir J *et al* (2015) RSPH3 Mutations Cause Primary Ciliary Dyskinesia with Central-
805 Complex Defects and a Near Absence of Radial Spokes. *Am J Hum Genet* 97: 153-162
806 Jumper J, Evans R, Pritzel A, Green T, Figurnov M, Ronneberger O, Tunyasuvunakool K, Bates R,
807 Zidek A, Potapenko A *et al* (2021) Highly accurate protein structure prediction with AlphaFold.
808 *Nature* 596: 583-589
809 Kherraf ZE, Amiri-Yekta A, Dacheux D, Karaouzene T, Coutton C, Christou-Kent M, Martinez G,
810 Landrein N, Le Tanno P, Fourati Ben Mustapha S *et al* (2018) A Homozygous Ancestral SVA-
811 Insertion-Mediated Deletion in WDR66 Induces Multiple Morphological Abnormalities of the
812 Sperm Flagellum and Male Infertility. *Am J Hum Genet* 103: 400-412
813 Knowles MR, Ostrowski LE, Leigh MW, Sears PR, Davis SD, Wolf WE, Hazucha MJ, Carson JL,
814 Olivier KN, Sagel SD *et al* (2014) Mutations in RSPH1 cause primary ciliary dyskinesia with a
815 unique clinical and ciliary phenotype. *Am J Respir Crit Care Med* 189: 707-717
816 Kott E, Legendre M, Copin B, Papon JF, Dastot-Le Moal F, Montantin G, Duquesnoy P, Piterboth
817 W, Amram D, Bassinet L *et al* (2013) Loss-of-function mutations in RSPH1 cause primary ciliary
818 dyskinesia with central-complex and radial-spoke defects. *Am J Hum Genet* 93: 561-570
819 Krause I, Pohler U, Grosse S, Shebl O, Petek E, Chandra A, Ebner T (2016) Characterization of the
820 injection funnel during intracytoplasmic sperm injection reflects cytoplasmic maturity of the
821 oocyte. *Fertil Steril* 106: 1101-1106
822 Kremer JR, Mastrorade DN, McIntosh JR (1996) Computer visualization of three-dimensional
823 image data using IMOD. *J Struct Biol* 116: 71-76
824 Kubo S, Yang SK, Black CS, Dai D, Valente-Paterno M, Gaertig J, Ichikawa M, Bui KH (2021)
825 Remodeling and activation mechanisms of outer arm dyneins revealed by cryo-EM. *EMBO Rep*
826 22: e52911
827 Kumar S, Stecher G, Tamura K (2016) MEGA7: Molecular Evolutionary Genetics Analysis Version
828 7.0 for Bigger Datasets. *Mol Biol Evol* 33: 1870-1874
829 Lek M, Karczewski KJ, Minikel EV, Samocha KE, Banks E, Fennell T, O'Donnell-Luria AH, Ware JS,
830 Hill AJ, Cummings BB (2016) Analysis of protein-coding genetic variation in 60,706 humans.
831 *Nature* 536: 285-291
832 Leung MR, Roelofs MC, Ravi RT, Maitan P, Henning H, Zhang M, Bromfield EG, Howes SC,
833 Gadella BM, Bloomfield-Gadelha H *et al* (2021) The multi-scale architecture of mammalian
834 sperm flagella and implications for ciliary motility. *EMBO J* 40: e107410

- 835 Li H (2013) Aligning sequence reads, clone sequences and assembly contigs with BWA-MEM.
836 *arXiv preprint arXiv:13033997*
- 837 Lin J, Heuser T, Carbajal-Gonzalez BI, Song K, Nicastro D (2012) The structural heterogeneity of
838 radial spokes in cilia and flagella is conserved. *Cytoskeleton (Hoboken)* 69: 88-100
- 839 Lin J, Yin W, Smith MC, Song K, Leigh MW, Zariwala MA, Knowles MR, Ostrowski LE, Nicastro D
840 (2014) Cryo-electron tomography reveals ciliary defects underlying human RSPH1 primary ciliary
841 dyskinesia. *Nat Commun* 5: 5727
- 842 Liu S, Zhang J, Kherraf ZE, Sun S, Zhang X, Cazin C, Coutton C, Zouari R, Zhao S, Hu F *et al* (2021)
843 CFAP61 is required for sperm flagellum formation and male fertility in human and mouse.
844 *Development* 148
- 845 Ma A, Zeb A, Ali I, Zhao D, Khan A, Zhang B, Zhou J, Khan R, Zhang H, Zhang Y *et al* (2021) Biallelic
846 Variants in CFAP61 Cause Multiple Morphological Abnormalities of the Flagella and Male
847 Infertility. *Front Cell Dev Biol* 9: 803818
- 848 Manichaikul A, Mychaleckyj JC, Rich SS, Daly K, Sale M, Chen W-M (2010) Robust relationship
849 inference in genome-wide association studies. *Bioinformatics* 26: 2867-2873
- 850 Martinez G, Beurois J, Dacheux D, Cazin C, Bidart M, Kherraf ZE, Robinson DR, Satre V, Le Gac G,
851 Ka C *et al* (2020) Biallelic variants in MAATS1 encoding CFAP91, a calmodulin-associated and
852 spoke-associated complex protein, cause severe astheno-teratozoospermia and male infertility.
853 *J Med Genet* 57: 708-716
- 854 Mastronarde DN (2005) Automated electron microscope tomography using robust prediction of
855 specimen movements. *J Struct Biol* 152: 36-51
- 856 McKenna A, Hanna M, Banks E, Sivachenko A, Cibulskis K, Kernytsky A, Garimella K, Altshuler D,
857 Gabriel S, Daly M (2010) The Genome Analysis Toolkit: a MapReduce framework for analyzing
858 next-generation DNA sequencing data. *Genome research* 20: 1297-1303
- 859 Nawaz S, Ullah MI, Hamid BS, Nargis J, Nawaz M, Hussain S, Ahmad W (2021) A loss-of-function
860 variant in DNA mismatch repair gene MLH3 underlies severe oligozoospermia. *J Hum Genet* 66:
861 725-730
- 862 Nicastro D, Schwartz C, Pierson J, Gaudette R, Porter ME, McIntosh JR (2006) The molecular
863 architecture of axonemes revealed by cryoelectron tomography. *Science* 313: 944-948
- 864 Organization WH (2010) *WHO laboratory manual for the examination and processing of human*
865 *semen*. World Health Organization, Geneva
- 866 Padma P, Satouh Y, Wakabayashi K, Hozumi A, Ushimaru Y, Kamiya R, Inaba K (2003)
867 Identification of a novel leucine-rich repeat protein as a component of flagellar radial spoke in
868 the Ascidian *Ciona intestinalis*. *Mol Biol Cell* 14: 774-785
- 869 Pigino G, Bui KH, Maheshwari A, Lupetti P, Diener D, Ishikawa T (2011) Cryoelectron tomography
870 of radial spokes in cilia and flagella. *J Cell Biol* 195: 673-687
- 871 Ralston KS, Lerner AG, Diener DR, Hill KL (2006) Flagellar motility contributes to cytokinesis in
872 *Trypanosoma brucei* and is modulated by an evolutionarily conserved dynein regulatory system.
873 *Eukaryot Cell* 5: 696-711
- 874 Rao Q, Han L, Wang Y, Chai P, Kuo YW, Yang R, Hu F, Yang Y, Howard J, Zhang K (2021) Structures
875 of outer-arm dynein array on microtubule doublet reveal a motor coordination mechanism. *Nat*
876 *Struct Mol Biol* 28: 799-810
- 877 Rohou A, Grigorieff N (2015) CTFFIND4: Fast and accurate defocus estimation from electron
878 micrographs. *J Struct Biol* 192: 216-221
- 879 Satouh Y, Inaba K (2009) Proteomic characterization of sperm radial spokes identifies a novel
880 spoke protein with an ubiquitin domain. *FEBS Lett* 583: 2201-2207

881 Schindelin J, Arganda-Carreras I, Frise E, Kaynig V, Longair M, Pietzsch T, Preibisch S, Rueden C,
882 Saalfeld S, Schmid B *et al* (2012) Fiji: an open-source platform for biological-image analysis. *Nat*
883 *Methods* 9: 676-682

884 Shamseldin HE, Shaheen R, Ewida N, Bubshait DK, Alkuraya H, Almardawi E, Howaidi A, Sabr Y,
885 Abdalla EM, Alfaifi AY *et al* (2020) The morbid genome of ciliopathies: an update. *Genet Med* 22:
886 1051-1060

887 Shen Q, Martinez G, Liu H, Beurois J, Wu H, Amiri-Yekta A, Liang D, Kherraf ZE, Bidart M, Cazin C
888 *et al* (2021) Bi-allelic truncating variants in CFAP206 cause male infertility in human and mouse.
889 *Hum Genet* 140: 1367-1377

890 Sironen A, Shoemark A, Patel M, Loebinger MR, Mitchison HM (2020) Sperm defects in primary
891 ciliary dyskinesia and related causes of male infertility. *Cell Mol Life Sci* 77: 2029-2048

892 Slabbert M, du Plessis SS, Huyser C (2015) Large volume cryoprotectant-free vitrification: an
893 alternative to conventional cryopreservation for human spermatozoa. *Andrologia* 47: 594-599

894 Smith EF, Sale WS (1992) Regulation of dynein-driven microtubule sliding by the radial spokes in
895 flagella. *Science* 257: 1557-1559

896 Smith EF, Yang P (2004) The radial spokes and central apparatus: mechano-chemical transducers
897 that regulate flagellar motility. *Cell Motil Cytoskeleton* 57: 8-17

898 Soraggi S, Riera M, Meyts R-D, Schierup MH, Almstrup K (2021) Evaluating genetic causes of
899 azoospermia: What can we learn from a complex cellular structure and single-cell
900 transcriptomics of the human testis? *Human Genetics* 140: 183-201

901 Toure A, Martinez G, Kherraf ZE, Cazin C, Beurois J, Arnoult C, Ray PF, Coutton C (2021) The
902 genetic architecture of morphological abnormalities of the sperm tail. *Hum Genet* 140: 21-42

903 Urbanska P, Song K, Joachimiak E, Krzemien-Ojak L, Koprowski P, Hennessey T, Jerka-Dziadosz
904 M, Fabczak H, Gaertig J, Nicastro D *et al* (2015) The CSC proteins FAP61 and FAP251 build the
905 basal substructures of radial spoke 3 in cilia. *Mol Biol Cell* 26: 1463-1475

906 Van der Auwera GA, Carneiro MO, Hartl C, Poplin R, Del Angel G, Levy-Moonshine A, Jordan T,
907 Shakir K, Roazen D, Thibault J (2013) From FastQ data to high-confidence variant calls: the
908 genome analysis toolkit best practices pipeline. *Current protocols in bioinformatics* 43: 11.10.
909 11-11.10. 33

910 Viswanadha R, Sale WS, Porter ME (2017) Ciliary Motility: Regulation of Axonemal Dynein
911 Motors. *Cold Spring Harb Perspect Biol* 9

912 Witman GB, Plummer J, Sander G (1978) Chlamydomonas flagellar mutants lacking radial spokes
913 and central tubules. Structure, composition, and function of specific axonemal components. *J*
914 *Cell Biol* 76: 729-747

915 Yang H, Wang H, Jaenisch R (2014) Generating genetically modified mice using CRISPR/Cas-
916 mediated genome engineering. *Nature protocols* 9: 1956-1968

917 Yang P, Diener DR, Yang C, Kohno T, Pazour GJ, Dienes JM, Agrin NS, King SM, Sale WS, Kamiya R
918 *et al* (2006) Radial spoke proteins of Chlamydomonas flagella. *J Cell Sci* 119: 1165-1174

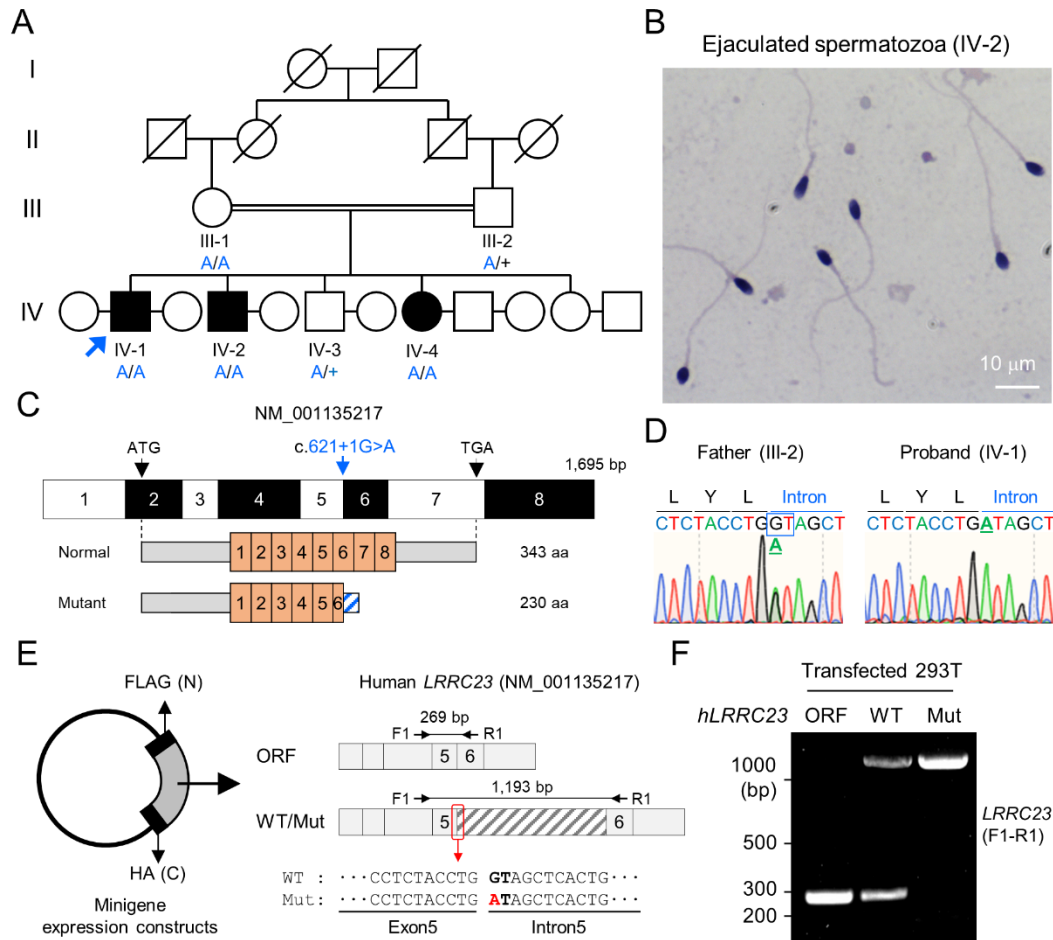
919 Yin W, Livraghi-Butrico A, Sears PR, Rogers TD, Burns KA, Grubb BR, Ostrowski LE (2019) Mice
920 with a Deletion of Rsph1 Exhibit a Low Level of Mucociliary Clearance and Develop a Primary
921 Ciliary Dyskinesia Phenotype. *Am J Respir Cell Mol Biol* 61: 312-321

922 Yoke H, Ueno H, Narita A, Sakai T, Horiuchi K, Shingyoji C, Hamada H, Shinohara K (2020) Rsph4a
923 is essential for the triplet radial spoke head assembly of the mouse motile cilia. *PLoS Genet* 16:
924 e1008664

925 Zhang X, Sun J, Lu Y, Zhang J, Shimada K, Noda T, Zhao S, Koyano T, Matsuyama M, Zhou S *et al*
926 (2021) LRRC23 is a conserved component of the radial spoke that is necessary for sperm motility
927 and male fertility in mice. *J Cell Sci* 134
928 Zhao Y, Pinsky J, Lin J, Yin W, Sears PR, Daniels LA, Zariwala MA, Knowles MR, Ostrowski LE,
929 Nicastro D (2021) Structural insights into the cause of human RSPH4A primary ciliary dyskinesia.
930 *Mol Biol Cell* 32: 1202-1209
931 Zheng S, Wolff G, Greenan G, Chen Z, Faas FGA, Barcena M, Koster AJ, Cheng Y, Agard DA (2022)
932 AreTomo: An integrated software package for automated marker-free, motion-corrected cryo-
933 electron tomographic alignment and reconstruction. *J Struct Biol X* 6: 100068
934 Zheng SQ, Palovcak E, Armache J-P, Cheng Y, Agard DA (2016) Anisotropic correction of beam-
935 induced motion for improved single-particle electron cryo-microscopy. *bioRxiv*: 061960
936 Zheng W, Li F, Ding Z, Liu H, Zhu L, Xu C, Li J, Gao Q, Wang Y, Fu Z *et al* (2021) Distinct
937 architecture and composition of mouse axonemal radial spoke head revealed by cryo-EM. *Proc*
938 *Natl Acad Sci U S A* 118
939 Zhu X, Liu Y, Yang P (2017) Radial Spokes-A Snapshot of the Motility Regulation, Assembly, and
940 Evolution of Cilia and Flagella. *Cold Spring Harb Perspect Biol* 9
941 Zivanov J, Otón J, Ke Z, von Kugelgen A, Pyle E, Qu K, Morado D, Castano-Dez D, Zanetti G,
942 Bharat TAM *et al* (2022) A Bayesian approach to single-particle electron cryo-tomography in
943 RELION-4.0. *bioRxiv*: 2022.2002.2028.482229
944 Zou W, Lv Y, Liu ZI, Xia P, Li H, Jiao J (2020) Loss of Rsph9 causes neonatal hydrocephalus with
945 abnormal development of motile cilia in mice. *Sci Rep* 10: 12435

946

947 **Figure Legends**
948



949

950

951 **Figure 1. A bi-allelic splicing donor site variant in *LRRC23* was identified from**
952 **asthenozoospermia patients.**

953 **A** A consanguineous pedigree with two infertile males (IV-1 and IV-2). IV-1 was subjected
954 for WES (arrow). Genotypes of the variant (blue) in all family members included in this study (III-1,
955 III-2, IV-1, IV-2, IV-3, and IV-4) are confirmed by Sanger sequencing. +, wild-type allele. An
956 infertile female sibling (IV-4) is marked in black circle.

957 **B** Papanicolaou-stained sperm from the infertile male (IV-2).

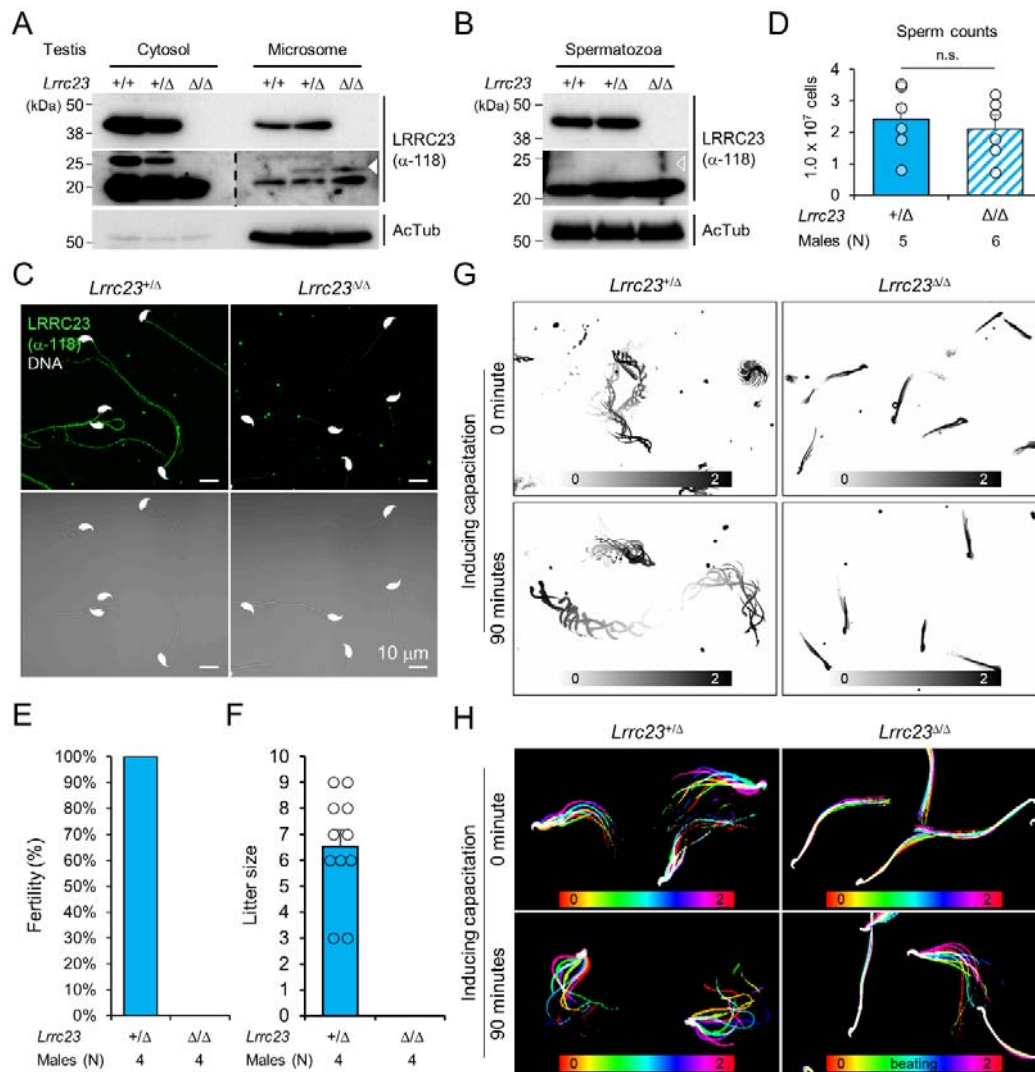
958 **C** Mapping of the *LRRC23* variant. Mutation of G to A at the splicing donor site in the 5th
959 intron is predicted to prevent *LRRC23* mRNA from splicing.

960 **D** Sequencing chromatograms presenting the *LRRC23* variant in the infertile male (IV-1)
961 and his father (III-2). The variant is underlined and normal splicing donor site (GT) is boxed.

962 **E, F** Minigene assay for testing altered splicing of *LRRC23* by the variant. (E) Minigene
963 constructs expressing *LRRC23* ORF containing the 5th intron (sashed) with wild-type (WT) or
964 mutant (Mut, red) splicing donor site were generated. The constructs are tagged with FLAG and

965 HA at N- and C-termini, respectively. (F) RT-PCR of the 293T cells transfected with the minigene
966 constructs reveals the 5th intron is not spliced out and retained by the variant. Intron-spanning
967 primers, F1 and R1, are used. Repeated three times with biological replications.

968



969

970 **Figure 2. *Lrrc23* mutant mice mimicking human splice variant phenocopy male infertility**
 971 **and reduced sperm motility.**

972 A, B Immunoblotting of LRRC23 in testis (A) and epididymal sperm (B) from mutant male mice.
 973 Truncated LRRC23 (arrowheads) is detected from testis microsomes (filled), but not in
 974 mature sperm (empty), of heterozygous (+/Δ) and homozygous (Δ/Δ) males. Acetylated tubulin
 975 (AcTub) is a loading control. Experiments were performed with three biological replications.

976 C Confocal images of immunostained LRRC23 in *Lrrc23*^{+/Δ} and *Lrrc23*^{Δ/Δ} epididymal sperm
 977 Experiments were repeated with three biological replications.

978 D Epididymal sperm counts. n.s., not significant.

979 E Pregnancy rate of *Lrrc23*^{+/Δ} and *Lrrc23*^{Δ/Δ} males.

980 F Number of litters from fertile females mated with *Lrrc23*^{+/Δ} and *Lrrc23*^{Δ/Δ} males.

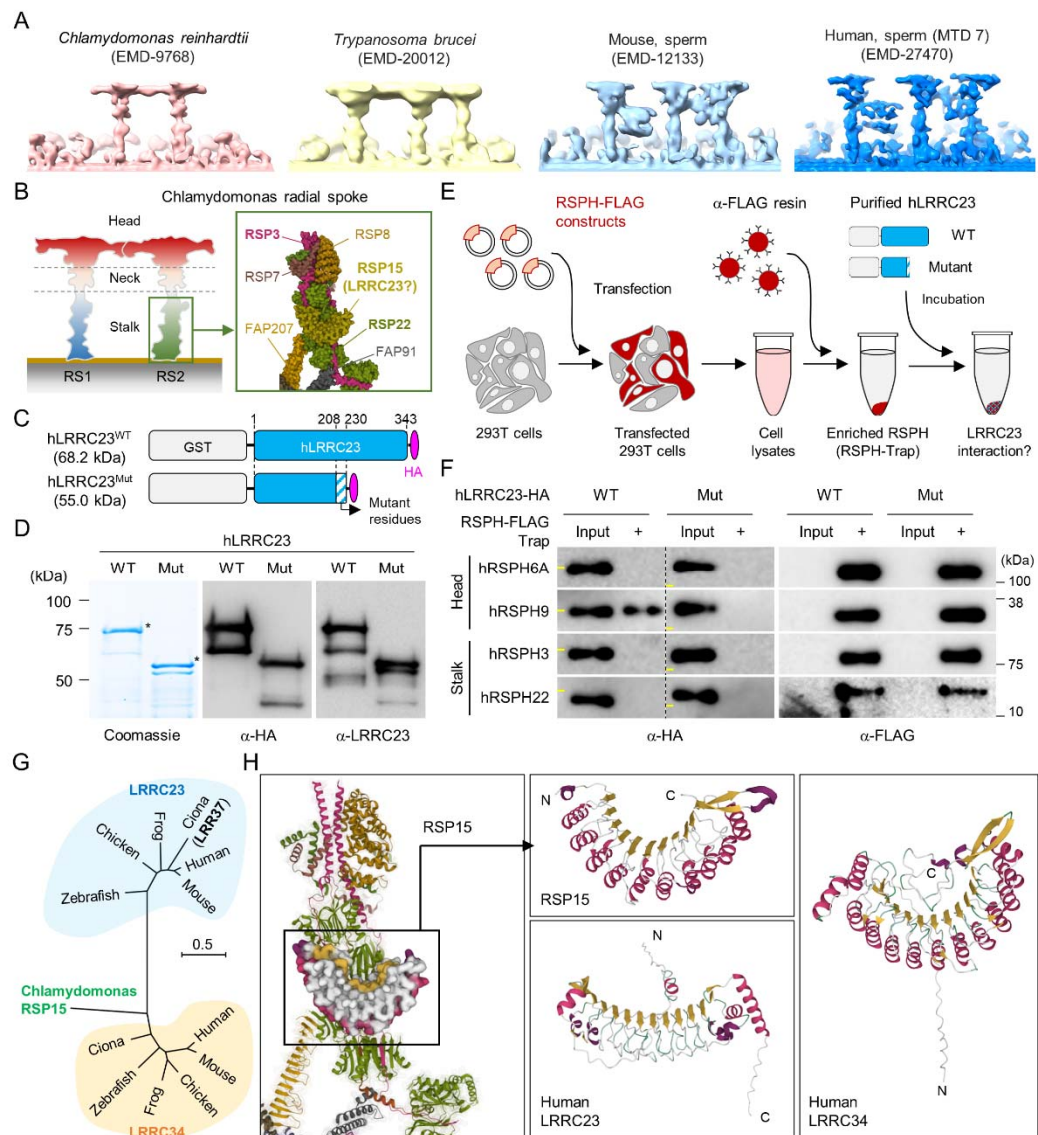
981 G Swimming trajectory of *Lrrc23*^{+/Δ} and *Lrrc23*^{Δ/Δ} sperm in viscous media (0.3%
 982 methylcellulose). Swimming trajectory for 2 seconds is overlaid. Experiments were performed

983 with three biological replications. See Movie [EV1](#).

984 H Flagellar waveforms of *Lrrc23*^{+/ Δ} and *Lrrc23* ^{Δ / Δ} sperm before (0 minute) and after (90
985 minutes) inducing capacitation. Flagellar movements for two beat cycles are overlaid and color
986 coded in time. Experiments were performed with three biological replications. See Movie [EV2](#).

987 Data information: In (A-C), samples from WT were used for positive or negative control of normal
988 or truncated LRRC23. In (D, F), circles indicate sperm counts from individual males (D) and pup
989 numbers from each litter (F), and data represented as mean \pm SEM (D, Mann-whiteny U test; F,
990 Student's t-test). n.s., non-significant.

991



992

993 **Figure 3. C-terminal truncation of human LRRC23 by the splicing site mutation prevents its**
 994 **interaction with radial spoke (RS) head.**

995 **A** Sub-tomogram averaging images of RSs from *Chlamydomonas reinhardtii* (red),
 996 *Trypanosoma brucei* (yellow), mouse sperm (sky blue), and human sperm (blue). RSs at 7th
 997 microtubule doublet (MTD) are shown for human sperm. Original data from Electron Microscopy
 998 Data Bank was rendered.

999 **B** Structure of RS in *C. reinhardtii*. A schematic cartoon shows the RS1 and 2. The structure of
 1000 RS2 stalk is shown in inset (PDB Id: 7JRJ).

1001 **C, D** Purification of normal (hLRRC23^{WT}) and the mutant human LRRC23 (hLRRC23^{Mut}) by the
 1002 splicing site mutation (c.621+1G>A) in this study. (C) Diagrams for the purified recombinant
 1003 normal and mutant proteins tagged with tagged with GST and HA at N- and C-termini,
 1004 respectively. (D) Purified proteins by Coomassie blue staining (*left*) and immunoblotting with α-HA
 1005 (*middle*) and α-LRRC23 (*right*). Proteins matched to the predicted size were marked with

1006 asterisks.

1007 E A cartoon of the RSPH-trap approach to test LRRC23 interaction with RS proteins.
1008 Individual human RS proteins tagged with FLAG (RSPH-FLAG) are expressed in 293T cells and
1009 enriched by α -FLAG resin from cell lysates. The recombinant RSPH proteins were incubated with
1010 the purified hLRRC23^{WT} or hLRRC23^{Mut} and subjected to immunoblotting.

1011 F Interaction of hLRRC23 to a RS head component, RSPH9. The purified hLRRC23 were
1012 incubated with the RSPH-Trap (RS head, RSPH6A and RSPH9; stalk, RSPH3 and RSPH22) and
1013 subjected to immunoblotting. 5% amount of the hLRRC23s used for the trap assay were loaded
1014 as inputs. Yellow lines in individual α -HA blot images indicate marker information (75 kDa, *left*, 50
1015 kDa, *right*). Experiments were repeated four times. Purified GST was used for negative control
1016 ([Fig EV4B](#)). Experiments were repeated three times with biological replications.

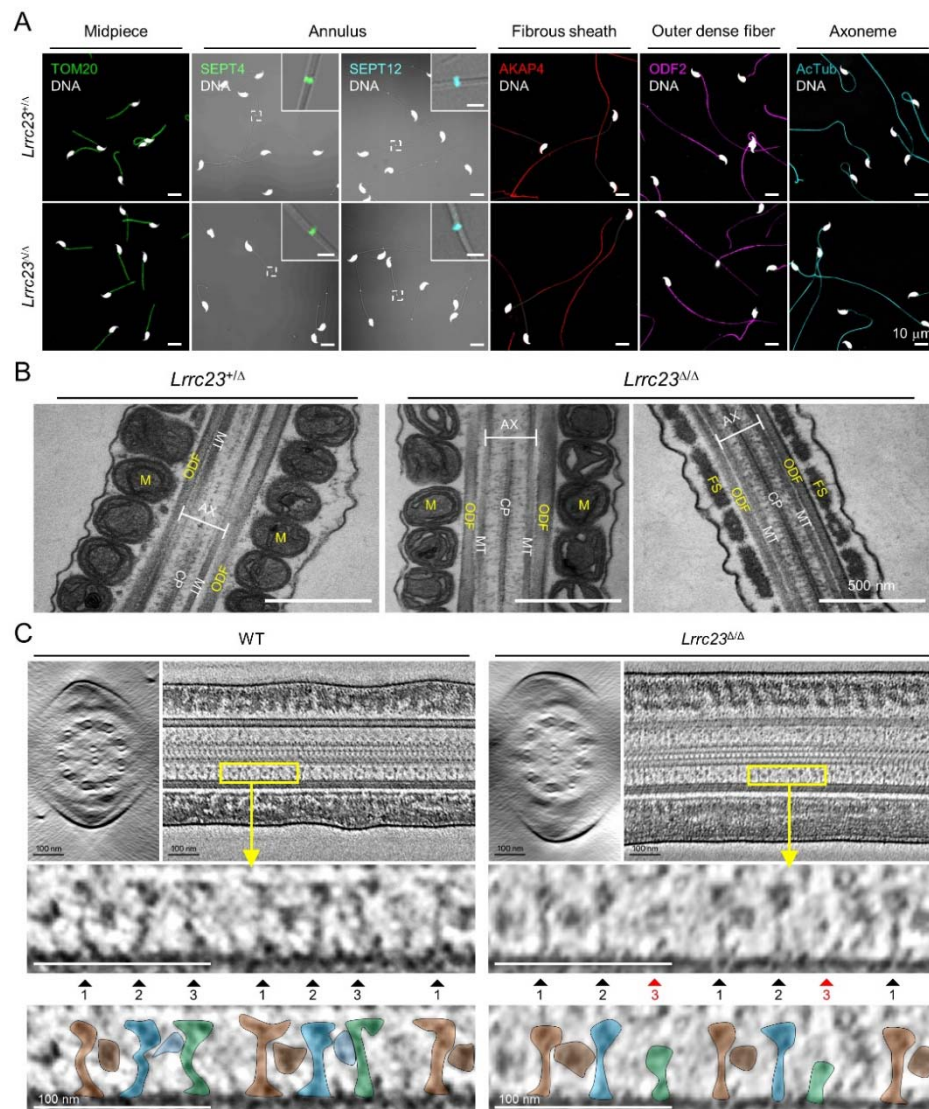
1017

1018 G A phylogenetic tree constructed by Maximum-likelihood analysis of the protein sequences
1019 of the *C. reinhardtii* RSP15 and the orthologs of LRRC23 and LRRC34. LRR37, the first LRRC23
1020 ortholog identified in *Ciona intestinalis* is marked in bold.

1021 H Comparison of the reported RSP15 from *C. reinhardtii* and the predicted structure of
1022 LRRC23 and LRRC34 from human. Atomic structure of the *C. reinhardtii* RS2 containing RSP15
1023 are represented by ribbon (RS2) and surface (RSP15) diagram (*left*, PDB Id: 7JU4). Ribbon
1024 diagrams of *C. reinhardtii* RSP15 and AlphaFold-predicted human LRRC23 (*middle*) and LRRC34
1025 (*right*) are shown for structural comparison. Secondary structures are color-coded. Different from
1026 *C. reinhardtii* RSP15 and LRRC34, LRRC23 does not display repeated α -helix (magenta)
1027 between β -sheets (gold).

1028

1029



1030

1031 **Figure 4. LRRC23 mutation disrupts the third radial spoke (RS) in sperm flagellum.**

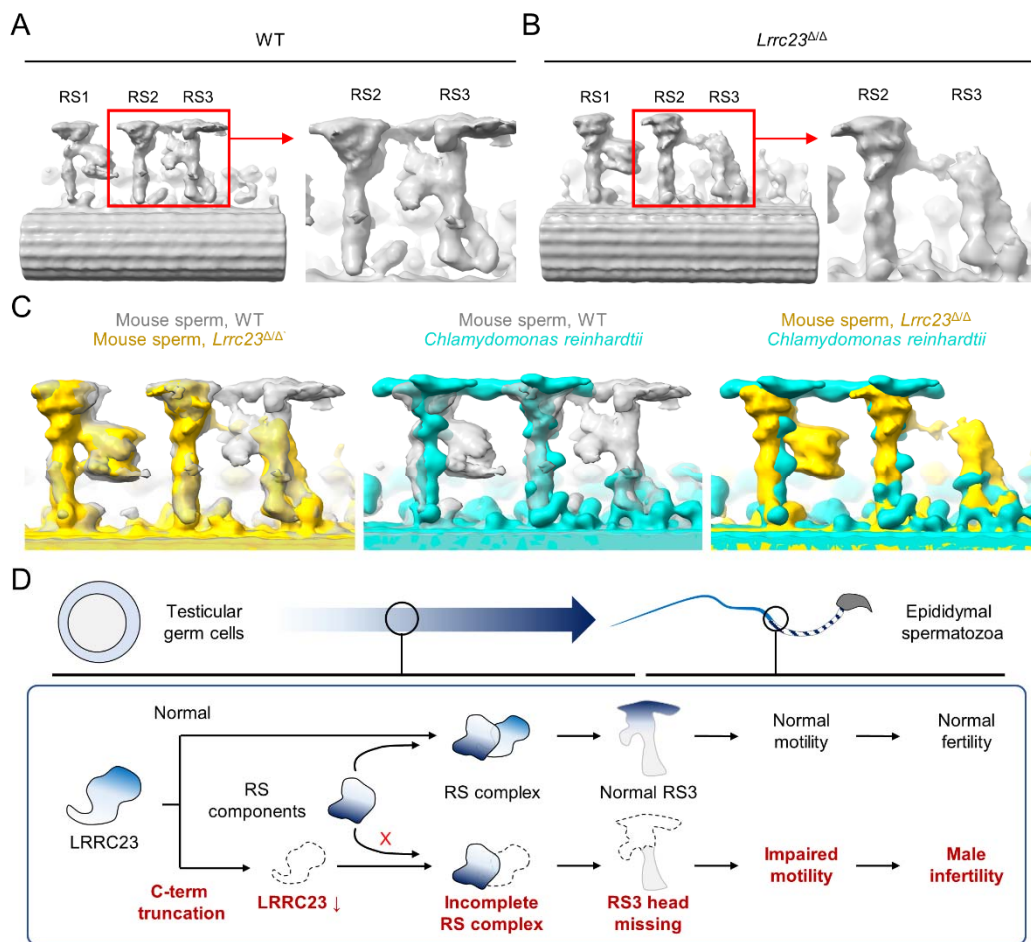
1032 A Immunostaining of flagellar proteins in different compartments. Shown are midpiece
 1033 (TOM20), annulus (SEPT4 and SEPT12), fibrous sheath (AKAP4), outer dense fiber (ODF2), and
 1034 axoneme (acetylated tubulin, AcTub) in *Lrrc23*^{+/ Δ} (top) and *Lrrc23* ^{Δ / Δ} (bottom) sperm. Magnified
 1035 insets are represented for annulus proteins (scale bars in insets = 2 μ m). Fluorescence and
 1036 corresponding DIC images are merged. Sperm heads were counter stained with Hoechst.
 1037 *Lrrc23*^{+/ Δ} sperm were used for positive control. Experiments were performed with three biological
 1038 replications.

1039 B Transmission electron microscopy images of *Lrrc23*^{+/ Δ} (left) and *Lrrc23* ^{Δ / Δ} (right) sperm.
 1040 Shown are longitudinal section of sperm flagella. M, mitochondria; ODF, outer dense fiber; AX,
 1041 axoneme; CP, central pair; MT, microtubule; FS, fibrous sheath. *Lrrc23*^{+/ Δ} sperm were used for
 1042 positive control.

1043 C Cryo-electron tomography (cryo-ET) of WT and *Lrrc23* ^{Δ / Δ} sperm flagella. Shown are
 1044 representative tomographic slices from WT (left) and *Lrrc23* ^{Δ / Δ} sperm (right). The 9+2 axonemal

1045 structure are shown in both WT and *Lrrc23*^{ΔΔ} in cross-sectional view (*left*). Axonemal structures
1046 are shown with proximal side of the flagellum on the left in longitudinal view (*right*; see Movie
1047 [EV3](#)). Magnified insets (*bottom*) reveal that RS1, 2, and 3 are shown in WT sperm (*left*, filled
1048 arrowheads) but RS3, especially head part, is not clearly visible (*right*, red arrowheads) in
1049 *Lrrc23*^{ΔΔ} sperm. RS1, 2, and 3 are distinguished by the interval between each set of RS1, 2, and
1050 3, and the electron dense area corresponding to the barrel (RS1) and bridge (RS2-3) structures.
1051 WT sperm were used for positive control.

1052



1053

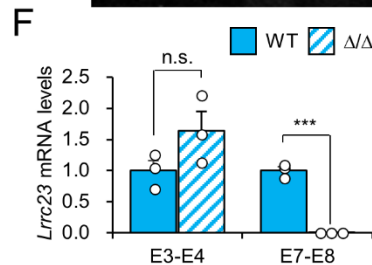
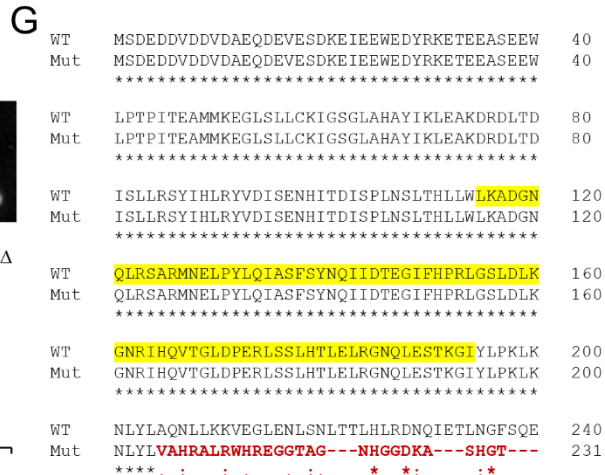
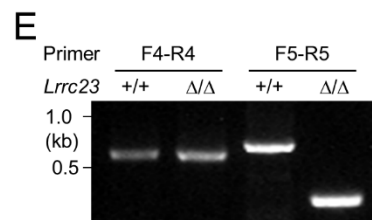
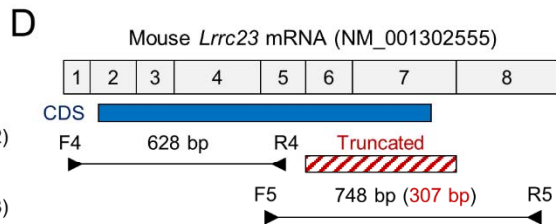
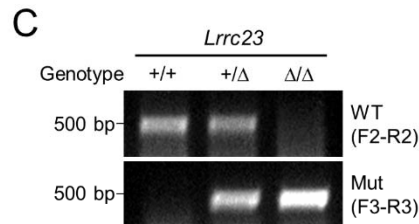
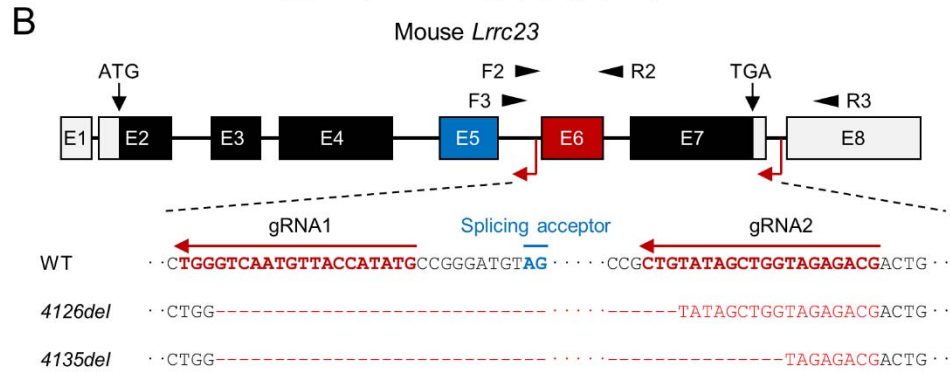
1054 **Figure 5. Head of the third radial spoke is absent in *Lrrc23^{Δ/Δ}* sperm flagella.**

1055 A, B Sub-tomogram averaging (STA) to analyze structural defects at radial spoke (RS) of WT
1056 (A) and *Lrrc23^{Δ/Δ}* sperm (B). Shown are STA images resulted from 96-nm doublet repeats from
1057 WT and *Lrrc23^{Δ/Δ}* sperm. RS2 and 3 are magnified and density to represent RS3 head and the
1058 bridge between RS2 and RS3 (red circle) is missed in *Lrrc23^{Δ/Δ}* sperm specifically.

1059 C Overwrapped STA images from 96 nm-doublet repeats from WT (gray) and *Lrrc23^{Δ/Δ}*
1060 (gold) sperm, and *Chlamydomonas reinhardtii* (cyan).

1061 D A proposed model of impaired sperm motility and male infertility by the LRRC23 loss of
1062 function.

1063



1078 **Figure EV2. Generation of LRRC23 mutant mouse models.**

1079 A A pair-wise alignment of human and mouse LRRC23 protein sequences. Deleted amino
1080 acids by the splice site mutation (encoded by exon 6 and 7) are written in red. Epitopes for the
1081 LRRC23 antibodies against N- (118-197, yellow) and C-terminus (209-288, cyan) are highlighted.

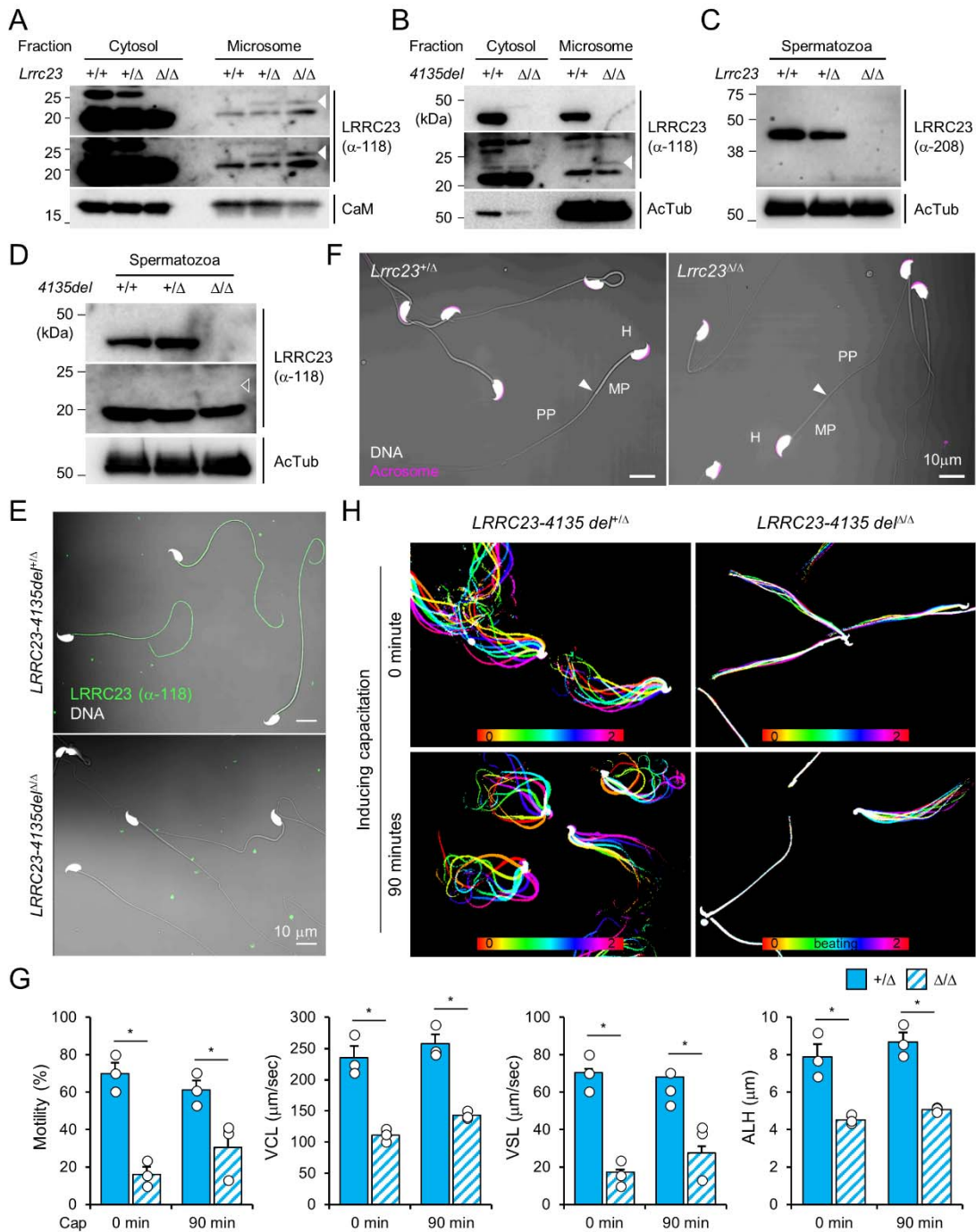
1082 B Generation of LRRC23 mutant mouse models by CRISPR/Cas9 genome editing. Two
1083 guide RNAs targeting 5th and 7th intron were used to generate mouse models expressing
1084 LRRC23 lacking C-terminus like the predicted human mutant LRRC23. Two mutant alleles with
1085 4126 (*Lrrc23-4126del*) or 4135 bp (*Lrrc23-4135del*) deletion were established.

1086 C Genotyping of the generated mouse models. Primer locations are marked in panel (B).
1087 *Lrrc23-4126del*^{Δ/Δ} and *Lrrc23-4135del*^{Δ/Δ} mice show the identical phenotypes. *Lrrc23-4126*^{Δ/Δ}
1088 mice were used as *Lrrc23*^{Δ/Δ} mice in this study unless indicated.

1089 D-F *Lrrc23* mRNA expression in testis from *Lrrc23* mutant males. (D) Shown is a diagram of
1090 exon composition of mouse *Lrrc23* mRNA (NM_001302555). Protein coding region (CDS),
1091 truncated exons in the mutant allele, and primers for RT-PCR are marked. A primer pair spanning
1092 truncated region (F5-R5) amplifies 748 bp and 307 bp PCR product from WT and the mutant
1093 alleles, respectively. (E) Endpoint and (F) real-time RT-PCR analyses of *Lrrc23* mRNA expression
1094 in *Lrrc23*^{Δ/Δ} testis. Primers amplifying exon 3 and 4 (E3-E4) and exon 7 and 8 (E7-E8) were used
1095 for real-time RT-PCR. Circles indicate relative levels from individual animals. N=3 for real-time
1096 PCR. Statistical analysis was performed by Student's t-test. n.s., not significant; *p****<0.001.

1097 G A pair-wise sequence alignment of WT and the predicted mutant LRRC23 proteins
1098 generated from the truncated allele. Non-native sequences from the truncated *Lrrc23* mRNA are
1099 colored in red.

1100



1101

1102

Figure EV3. Characterization of the *Lrrc23* loss of function male mice.

1103

1104

1105

1106

1107

A-D Protein expression of LRRC23 in wild type (WT) and *Lrrc23* mutant males. (A) Original images of truncated LRRC23 immunoblotting in testis shown in Fig. 2A. Short (top) and long (middle) exposure images are shown. Calmodulin (CaM) is a loading control. (B) Immunoblotting of LRRC23 in testis from *Lrrc23-4135del* mutant males. (C) LRRC23 immunoblotting in epididymal sperm from WT, *Lrrc23*^{+/Δ}, and *Lrrc23*^{Δ/Δ} males. (D) Immunoblotting of LRRC23 in WT

1108 and *Lrrc23-4135del^{ΔΔ}* sperm. Truncated LRRC23 (arrowheads) is detected from testis (filled, A
1109 and B), but not from epididymal sperm (empty, D) of *Lrrc23* mutant males. Acetylated tubulin
1110 (AcTub) is a loading control. Samples from WT males were used for either positive or negative
1111 controls of normal and truncated LRRC23, respectively (A, B, C, and D).

1112 E Confocal images of immunostained LRRC23 in *Lrrc23-4135del^{+Δ}* and *Lrrc23-4135del^{ΔΔ}*
1113 sperm.

1114 F Confocal images of epididymal sperm from *Lrrc23^{+Δ}* and *Lrrc23^{ΔΔ}* males. Acrosome is
1115 stained with wheat-germ agglutinin. Arrowheads indicate the annulus.

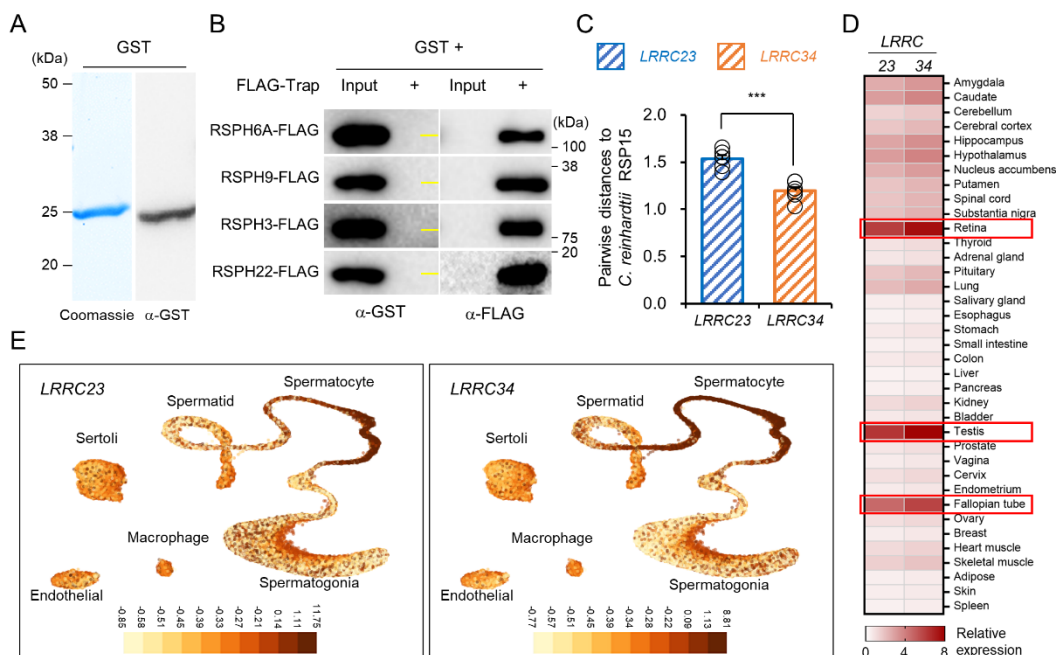
1116 G Computer assisted sperm analysis (CASA) to measure motility parameters of *Lrrc23^{+Δ}*
1117 and *Lrrc23^{ΔΔ}* sperm. Sperm motility parameters were measured before (0 min) and after (90 min)
1118 inducing capacitation. VCL, curvilinear velocity; VSL, straight line velocity; ALH, amplitude of
1119 lateral head. Mann-Whitney U test was used for statistical comparison. * $p \leq 0.05$. N=3. Circles
1120 indicate values from individual animals. Data is represented as mean \pm SEM.

1121 H Flagellar movement of the *Lrrc23-4135del^{+Δ}* (*left*) and *Lrrc23-4135del^{ΔΔ}* (*right*). Shown
1122 are overlays of sperm tail movement over two beat cycles before (0 min, *top*) and after (90 min,
1123 *bottom*) inducing capacitation.

1124 Used are LRRC23 antibodies recognizing N- (α -118) or C- (α -208) terminal region (A, B, C, D,
1125 and E). Hoechst is used for counterstaining DNA and fluorescence and DIC images are merged
1126 (E and F). All experiments were carried out with over three biological replications.

1127

1128



1129

1130 **Figure EV4. A predicted RSP15 ortholog, LRRC34, in metazoan species.**

1131 A Purified recombinant GST confirmed by Coomassie blue staining (left) and
1132 immunoblotting (right).

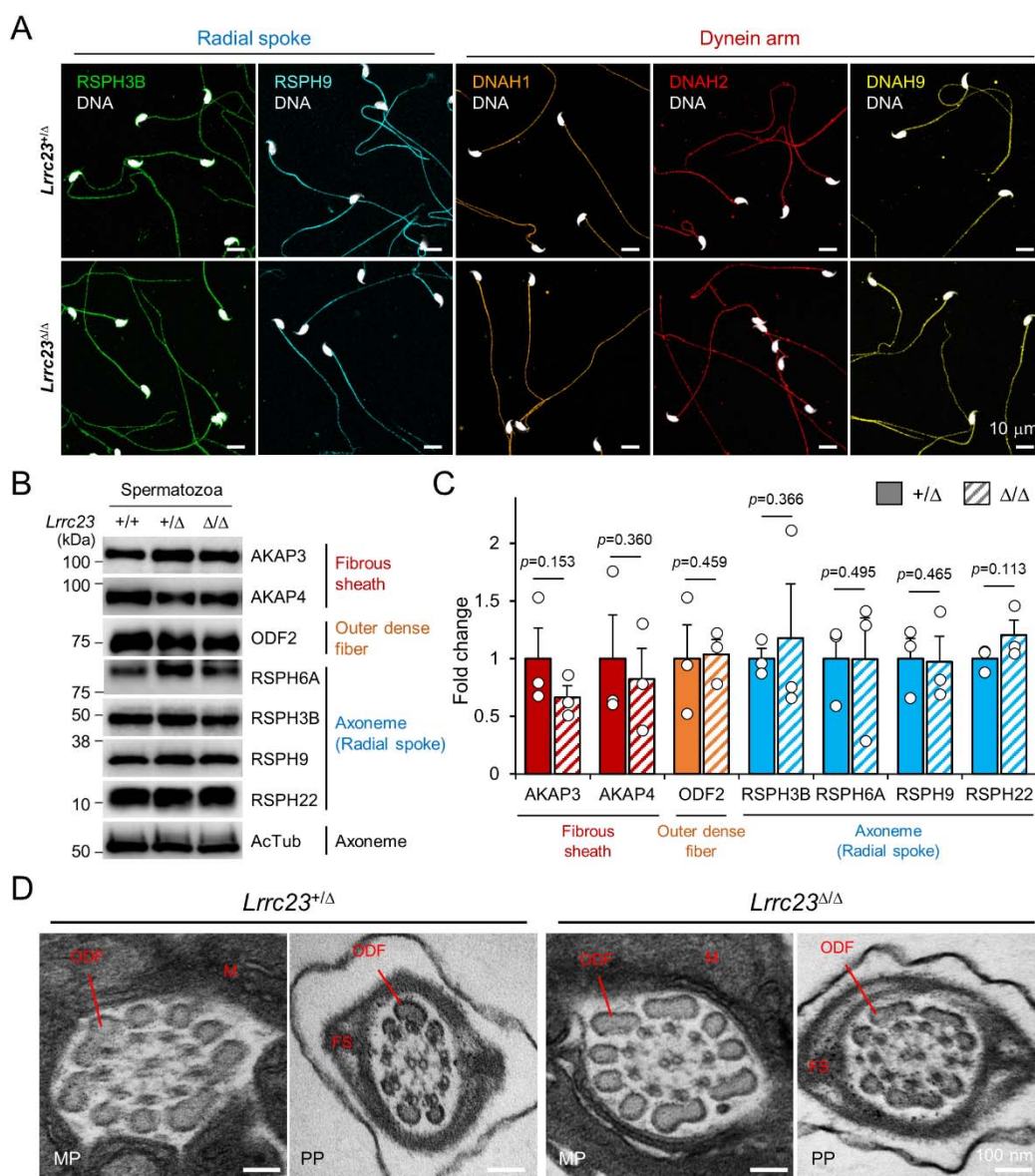
1133 B Interaction test of GST to human radial spoke proteins (RSPH) by trap-assay as a
1134 negative control. Yellow lines in α -GST blot images indicate molecular weight (25 kDa).

1135 C Comparison of the pairwise distances of *Chlamydomonas reinhardtii* RSP15 to the
1136 LRRC23 or LRRC34 orthologs. Protein sequences of *C. reinhardtii* RSP15 and the metazoan
1137 LRRC23 and LRRC34 orthologs were aligned and pairwise distances were calculated. Protein
1138 sequences of the *C. reinhardtii* RSP15 are closer to LRRC34 orthologs evolutionarily than
1139 LRRC23 orthologs in metazoan. Statistical analysis was performed by Student's t-test. *** $p < 0.001$,
1140 Data is represented by mean \pm SEM.

1141 D A heatmap to represent human tissue mRNA expression of LRRC23 and LRRC34.
1142 Relative mRNA expression levels were calculated by normalizing tissue nTPM values with the
1143 median values. Three tissues with the highest LRRC23 and LRRC34 mRNA levels are
1144 highlighted. RNA GTEX tissue gene data from The Human Cell Atlas was used.

1145 E LRRC23 (left) and LRRC34 (right) mRNA expression in human testicular cells. mRNA
1146 levels in individual cells are represented by UMAP plots downloaded from UCSC cell browser.

1147



1148

1149 **Figure EV5. Flagellar compartmentalization in *Lrrc23*-mutant sperm.**

1150 A Distribution of the axonemal components in *Lrrc23*^{Δ/Δ} sperm. Immunostained radial spoke
 1151 (RSPH3B and RSPH9) and dynein arm (DNAH1, DNAH2, and DNAH9) in *Lrrc23*^{+/ Δ} and *Lrrc23*^{Δ/Δ}
 1152 sperm are shown by confocal images. Hoechst is used for counterstaining the sperm head.
 1153 Experiment was performed with three biological replications.

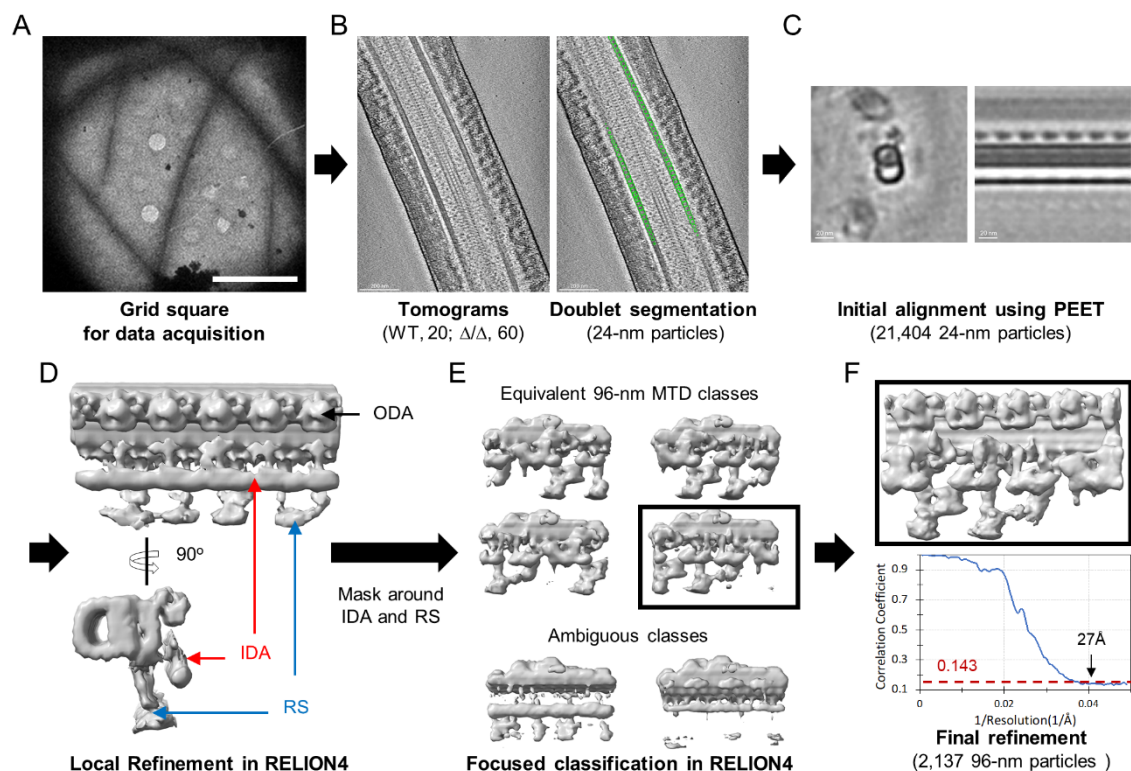
1154 B, C Unaffected protein levels of the representative components of fibrous sheath, outer
 1155 dense fiber, and axoneme in *Lrrc23*^{Δ/Δ} sperm. (B) Immunoblotting of the flagellar components in
 1156 cauda sperm. Acetylated tubulin (AcTub) is a loading control. (C) Fold-changes of the flagellar
 1157 components levels in *Lrrc23*^{+/ Δ} (filled) and *Lrrc23*^{Δ/Δ} (hatched) sperm. Relative protein levels were
 1158 quantified by measuring the band intensity and normalized by the AcTub intensity. The average
 1159 level of each protein in *Lrrc23*^{+/ Δ} sperm is set to 1-fold. Circles represents fold changes of each
 1160 sperm protein from individual males. Data represented as mean ± SEM. Statistical analysis was

1161 performed by Student's t-test. N=3.

1162 D Transmission electron microscopy (TEM) images of epididymal sperm from *Lrrc23*^{+/ Δ} and
1163 *Lrrc23* ^{Δ/Δ} males. Shown are representative cross section TEM images of *Lrrc23*^{+/ Δ} (*left*) and
1164 *Lrrc23* ^{Δ/Δ} (*right*) sperm. No obvious structural defects at the midpiece (MP) and principal piece
1165 (PP) were observed from and *Lrrc23* ^{Δ/Δ} sperm. M, mitochondria; FS, fibrous sheath; ODF, outer
1166 dense fiber; AX, axoneme.

1167 WT and/or *Lrrc23*^{+/ Δ} sperm were used for positive control (A, B, C and D).

1168



1169

1170 **Figure EV6. Workflow of cryo-electron tomography (cryo-ET) and sub-tomogram averaging**
 1171 **(STA) processing of 96-nm microtubule doublet repeat from mouse sperm.**

1172 **A** An example of low magnification map of *Lrrc23* ^{Δ/Δ} mouse sperm on grid square. Scale bar,
 1173 10 μ m.

1174 **B** An example tomographic slice obtained from sperm on the grid and segmented particles
 1175 with 24 nm interval (green circles, *right*).

1176 **C** Initial alignment using PEET. Cross-sectional (*left*) and longitudinal (*right*) views are
 1177 shown. **D** Local refinement of 24-nm particles in RELION4 after coordination and Euler
 1178 angles transform. Density for outer dynein arm (ODA, black arrow) are visualized. Densities to
 1179 represent inner dynein arm (IDA, red arrows) and radial spoke (RS, blue arrows) were averaged
 1180 due to symmetry mismatch.

1181 **E** A soft-edge mask around IDA and RS. 96-nm repeat of microtubule doublet (MTD)
 1182 classes with different translational symmetries (*top*) were obtained using focused classification in
 1183 RELION4. The ambiguous classes (*bottom*) were discarded.

1184 **F** Final local refinement using one 96-nm repeat class. The gold-standard Fourier Shell
 1185 Correlation (FSC) curve is shown at bottom.

1186

1187

1188 **Expanded View Tables and Movies**

1189

1190 **Table EV1. Clinical diagnosis of the infertile patients**

1191 **Table EV2. Variant Detail in the infertility Family**

1192 **Table EV3. Summarized imaging acquisition parameters and 3D refinement statistics**

1193

1194 **Movie EV1. *Lrrc23*^{+Δ} and *Lrrc23*^{ΔΔ} sperm swimming freely in a viscous environment.**

1195 Free-swimming *Lrrc23*^{+Δ} and *Lrrc23*^{ΔΔ} sperm in the viscous condition containing 0.3%
1196 methylcellulose were recorded for 2 seconds before and after inducing capacitation for 90
1197 minutes. Individual videos are played at 50 fps (1/2 speed).

1198 **Movie EV2. Flagellar waveform of *Lrrc23*^{+Δ} and *Lrrc23*^{ΔΔ} sperm before and after inducing**

1199 **capacitation.** Tail movements of head-tethered sperm from *Lrrc23*^{+Δ} and *Lrrc23*^{ΔΔ} males are
1200 recorded for 2 seconds before and after incubation under capacitating conditions for 90 minutes.
1201 Each video is played at 100 fps (1/2 speed).

1202 **Movie EV3. Tilted series of cryo-electron tomogram slices from WT (*left*) and *Lrrc23*^{ΔΔ}**

1203 **(*right*) spermatozoa.** Tomogram images were acquired of WT and *Lrrc23*^{ΔΔ} sperm were
1204 acquired on the grid and image slices were rendered to show the axonemal structure in a tilt
1205 series.

1206